1 # Structural and mechanistic insights into human choline transport

2 Tsai-Hsuan Weng[1], Ainara Claveras Cabezudo[2,3], Wiebke Jösting[1], Andre Bazzone[4], Sonja Welsch[5], Gonca Gursu[1], Gerhard

3 Hummer[2,6], Di Wu[1]*, Schara Safarian[1,7,8]*

4

5 **Affiliations**

6 [1] *Department of Molecular Membrane Biology, Max Planck Institute of Biophysics, D-60438 Frankfurt/Main, Germany*
7

8 [2] *Department of Theoretical Biophysics, Max Planck Institute of Biophysics, D-60438 Frankfurt/Main, Germany*
9

10 [3] *IMPRS on Cellular Biophysics, D-60438 Frankfurt/Main, Germany*
11

12 [4] *Nanion Technologies GmbH, Ganghoferstr. 70a, 80339, Munich, Germany*
13

14 [5] *Central Electron Microscopy Facility, Max Planck Institute of Biophysics, D-60438 Frankfurt am Main, Germany*
15

16 [6] *Institute of Biophysics, Goethe University Frankfurt, D-60438 Frankfurt/Main, Germany*
17

18 [7] *Department of Microbiology and Immunology, School of Biomedical Sciences, University of Otago, Dunedin, NZ-9054, New Zealand*
19

20 [8] *present address: Fraunhofer Institute for Translational Medicine and Pharmacology ITMP Frankfurt, D-60438 Frankfurt/Main, Germany*
21

22 *Correspondence and requests for materials should be addressed to Di Wu (di.wu@biophys.mpg.de) and Schara Safarian

23 (schara.safarian@biophys.mpg.de).

24

25

26 **Abstract**

27 Human feline leukaemia virus subgroup C receptor-related proteins 1 and 2 (FLVCR1 and 2) are major

28 facilitator superfamily transporters from the solute carrier family 49. Dysregulation of these ubiquitous

29 transporters has been linked to various haematological and neurological disorders. While both FLVCRs

30 were initially proposed to hold a physiological function in heme transport, subsequent studies

31 questioned this notion. Here, we used structural, computational and biochemical methods and

32 conclude that these two FLVCRs function as human choline transporters. We present cryo-electron

33 microscopy structures of FLVCRs in different inward- and outward-facing conformations, captured in

34 the apo state or in complex with choline in their translocation pathways. Our findings provide insights

35 into the molecular framework of choline coordination and transport, largely mediated by conserved

36 cation-$\pi$ interactions, and further illuminate the conformational dynamics of the transport cycle.

37 Moreover, we identified a heme binding site on the protein surface of the FLVCR2 N-domain, and

38 observed that heme actively drives the conformational transitions of the protein. This auxiliary binding

39 site might indicate a potential regulatory role of heme in the FLVCR2 transport mechanisms. Our work

40      resolves the contested substrate specificity of the FLVCRs, and sheds light on the process of maintaining

41      cellular choline homeostasis at the molecular level.

42 **Introduction**

43 The feline leukaemia virus subgroup C receptor (FLVCR) family, a member of the major facilitator

44 superfamily (MFS) of secondary active transporters, consists of four paralogues encoded by the human

45 *SLC49* gene group[1]. FLVCR1 (SLC49A1) was initially identified as the cell receptor for feline leukaemia

46 virus (FeLV), a retrovirus that causes profound anaemia in cats by interfering with erythropoiesis[2].

47 FLVCR2 (SLC49A2), another major member of the family, shares 60% sequence identity with FLVCR1 in

48 the transmembrane domain but does not bind to the feline leukaemia virus subgroup C envelope

49 protein[3]. Both transporters exhibit ubiquitous tissue distribution in humans and have significant

50 haemato- and neuropathological implications[1,4]. Dysfunction of FLVCR1 caused by germline mutations

51 is associated with posterior column ataxia with retinitis pigmentosa (PCARP)[5], while its alternatively

52 spliced isoforms have been linked to Diamond-Blackfan anaemia (DBA)[6]. Similarly, truncation and

53 missense mutations in the gene encoding for FLVCR2 are associated with the autosomal-recessive

54 cerebral proliferative vasculopathy known as Fowler syndrome[7,8]. Furthermore, both FLVCR variants

55 are suggested to play a key role in cell development and differentiation, including angiogenesis and

56 tumorigenesis[9–12].

57

58 Here, we studied the molecular architecture, the conformational landscape, and the contested

59 substrate specificity of human FLVCR1 and FLVCR2 using single-particle analysis cryogenic electron

60 microscopy (SPA cryo-EM) and molecular dynamics (MD) simulations. Our findings indicate that FLVCR1

61 and FLVCR2 both represent previously uncharacterized, ubiquitous human choline transporters.

62 **Results**

63 *Overall architecture of FLVCR1 and FLVCR2*

64 We stably integrated the human *SLC49A1* and *SLC49A2* genes into human embryonic kidney cells

65 (HEK293), and recombinantly produced wildtype FLVCR1a (hereafter referred to as FLVCR1) and FLVCR2

66 variants with C-terminal flag-tag modifications, respectively. Affinity-purified samples of each

67 transporter were subjected to SPA cryo-EM (Supplementary Fig. 1).

68

69 We determined the respective structures of apo FLVCR1 and FLVCR2 at 2.9 Å resolution, captured in

70 inward-facing conformations (Fig. 1a,b and Extended Data Fig. 1 and 2). Both FLVCR paralogs share a

71 common MFS-type architecture composed of 12 transmembrane $\alpha$-helices (TM) arranged into two

72 pseudo-symmetrical domains[13] (Fig. 1c). In both inward-facing structures, the N-domain (TM1-6) and

73 the C-domain (TM7-12) are connected by a long and flexible loop containing two short horizontal

74 helices (H1 and H2) on the inner side of the membrane (Fig. 1). On the inner side of FLVCR2, we resolved

75 a short helical segment at the C-terminus (H3), while the density of the FLVCR1 C-terminus was less

76 pronounced (Extended Data Fig. 3). Further, we identified an N-linked glycosylation site at N265 of

77 FLVCR1 which locates within the external loop connecting TMs 5 and 6 (EL5-6; Fig. 1a). This

78 glycosylation pattern is absent in the analogous site of the FLVCR2 structure.

79

80 The inward-facing conformations of FLVCR1 and FLVCR2 exhibit a close resemblance to each other, with

81 a root mean square deviation (C$\alpha$ r.m.s.d.) of 0.993 Å. Both structures feature a wedge-shaped solvent-

82 accessible cavity that is mainly created by the separation of TMs 4 and 5 of the N-domain from TMs 10

83 and 11 of the C-domain (Extended Data Fig. 4a). This space extends halfway across the membrane with

84 a similar depth of around 23 Å in both (Fig. 2c and Extended Data Fig. 4b). On the level of the outer

85 leaflet, TMs 1, 2, and 5 of the N-domain and TMs 7, 8, and 11 of the C-domain pack tightly against each

86 other and thus shield the central cavity from the external space (Extended Data Fig. 4a). Notably, TMs

87 1, 4, and 7 exhibit disordered regions at their C-terminal ends, followed by short kinked helical motifs

88 designated TMs 1b, 4b, and 7b (Fig. 1c and Extended Data Fig. 3).

89 *Conformational difference between inward- and outward-facing structures of FLVCR2*

90 From the as-isolated FLVCR2 samples we were able to determine not only the inward-facing

91 conformations but also the outward-facing conformation from class averages of even particle

92 distribution (Fig. 2a and Extended Data Fig. 2a). The outward-facing conformation of FLVCR2 is

93 characterized by a cavity that is accessible from the external space created by a rocker-switch rigid-

94 body motion of the two domains (Fig. 2b,c and Supplementary Video 1). This motion shifts the outer

95 halves of all TMs away from the central axis, while the inner halves adopt an inward movement to

96 obstruct the exit (Fig. 2b). The cavities in outward- and inward-facing conformations are 7.4 Å and 8.6

97 Å wide at their respective openings (Fig. 2c). The wedge-like volume of both cavities is surrounded by

98 an uncharged and hydrophobic protein environment, lined by mostly conserved residues (Extended

99 Data Fig. 5). Compared to the inward-facing cavity, the outward-facing cavity demonstrates a more

100 restricted pathway within its central region. In this narrowed segment of the cavity, the channel ends

101 at W102 and Y325, two residues that are highly conserved in both FLVCR transporters (Fig. 2c and

102 Extended Data Fig. 4b and 5).

103

104 In line with an alternating-access model, the inward-facing conformation of FLVCR2 features a tightly-

105 sealed external gate. This is mainly achieved by the juxtaposition of TM1b (N-domain) and TM7b (C-

106 domain; Fig. 2c,d). The inter-domain interaction between these two motifs is stabilized by a hydrogen

107 bonding network consisting of two pseudo-symmetry-related asparagine residues (N110-N332), as well

108 as E343 (TM8) and N239 (EL5-6; Supplementary Fig. 2). Furthermore, we identified a stable inter-

109 domain salt bridge between D124 (TM2) and R333 (TM7b), presumably reinforcing the external

110 occlusion (Fig. 2c,d, and Supplementary Fig. 2). FLVCR1 appears to employ a similar gating mechanism

111 on its external side, given that all the residues involved in the hydrogen bonding network of FLVCR2 are

112 found to be highly conserved between these two paralogs (Extended Data Fig. 4b,c). However, the

113 D124-R333 salt bridge in FLVCR2 is not conserved in FLVCR1. While the location of the D147 residue in

114 FLVCR1 aligns with that of D124 in FLVCR2, FLVCR1 possesses a glutamine taking the position of the

115 arginine (Extended Data Fig. 4c).

116

117    During the transition from inward- to outward-facing conformation of FLVCR2, interactions contributing

118    to the external gate become disrupted, while the formation of the internal gate occludes the central

119    cavity from the internal side. TM4b of the N-domain moves in proximity to the N-terminal end of TM11

120    of the C-domain to establish a first level of occlusion (Fig. 2b,c). An interaction network consisting of

121    several hydrogen bonds and a salt bridge is found within this region (Fig. 2e). E435 (TM11) plays a

122    central and versatile role by stably forming a hydrogen bond with S203 (TM4b) and a concurrent salt

123    bridge with R200 (TM4b; Fig. 2e and Supplementary Fig. 2). An additional inter-domain hydrogen

124    bonding site is identified between S199 (TM4b) and S439 (TM11; Fig. 2e and Supplementary Fig. 2). In

125    the peripheral region, K372 and R374 (EL8-9) approach N209 (EL4-5) and S212 (TM5) to form hydrogen

126    bond pairs and thus block the lateral accessibility of the cavity (Fig. 2e and Supplementary Fig. 2). A

127    second level of occlusion was observed beneath the internal ends of TMs 4, 10 and 11, where H1 and

128    H3 are positioned in close proximity (Fig. 2c,f). Here, the backbone carbonyl group and amide nitrogen

129    of A283 (H1) form stable hydrogen bonds with N497 (H3) and Y431 (IL10-11), respectively (Fig. 2f and

130    Supplementary Fig. 2). Together with the loop connecting TMs 10 and 11, the two helical motifs H1

131    and H3 serve as a latch to secure the closure of the two domains on the internal side.

132     *Substrate-specificity and auxiliary binding sites*

133     The transport substrates of both FLVCR1 and FLVCR2 have been contested for decades[14–17]. Both

134     FLVCR1 and FLVCR2 were previously proposed to hold a function in heme transport. With the goal of

135     assessing their heme-binding capabilities and localizing the putative heme-binding site, we performed

136     cryo-EM experiments using heme as a potential substrate.

137

138     A central observation upon determining the structure of heme-supplemented FLVCR2 was that the

139     presence of heme resolved the conformational heterogeneity, fully driving the transporter into the

140     outward-facing conformation (Fig. 3a and Extended Data Fig. 2b). Surprisingly, no density features of

141     heme were noticeable within the central cavity. Instead, we observed a density corresponding to heme

142     in the vicinity of the N-terminus of TM1 on the internal side, where it replaces the density we assigned

143     as a lipid molecule in the apo outward-facing structure (Fig. 3a,b). The protein surface in this particular

144     region displays a patch of positive charges, suggesting the heme molecule to be held in place by the

145     formation of electrostatic interactions between its two propionate groups and the side chains of R81,

146     R82, and K273 (Fig. 3b and Extended Data Fig. 5d). The map density of bound heme in our structure

147     indicates local mobility in the heme position due to the absence of macrocycle rigidifying axial

148     coordination (Fig. 3b). By contrast, cryo-EM studies on FLVCR1 in the presence of heme did not reveal

149     any heme binding or notable conformational changes. It is to note that neither the cavity dimensions

150     nor the residues lining the central cavities of FLVCR1 and FLVCR2 suggest the existence of a heme-

151     binding pocket.

152

153     To further characterize the molecular nature of heme binding in FLVCR2, we carried out atomistic MD

154     simulations, focusing on FLVCR2 in a lipid bilayer composed of 75% palmitoyloleoyl

155     phosphatidylethanolamine (POPE) and 25% palmitoyloleoyl phosphatidylglycerol (POPG). To probe

156     possible binding into the transport pathway, we first placed a heme close to the cavity opening in the

157     outward-facing conformation. In the subsequent MD simulations, the heme immediately crossed the

158     solvent layer and periodic boundary to interact with the loop region on the internal side for the

159    remainder of the simulation (Supplementary Video 2). We then positioned heme on the inner side of

160    the bilayer near the binding site observed by cryo-EM at the N-terminus of TM1 (Fig. 2c). In all replicas,

161    the contact between heme and the R82 residue was lost early in the simulations as the heme

162    reoriented and was absorbed into the lipid bilayer. However, the contact between one of the

163    propionate groups and R83 was consistently maintained. Upon membrane insertion, the heme formed

164    additional contacts with other residues (Supplementary Fig. 3). Stable interactions were observed

165    between the methyl group of heme and I270 (TM6), as well as one of the propionate groups and K273

166    (TM6). Our MD simulation data, together with our structural findings, point to the existence of a heme-

167    binding site at the N-domain of FLVCR2, located near the inner surface of the membrane. This finding

168    is in line with previously reported results demonstrating heme-binding at the N-terminal segment of

169    FLVCR2[18].

170

171    Subsequently, we focused our attention on choline as a potential substrate of FLVCR1 and FLVCR2 based

172    on the characteristic tryptophan-tyrosine clusters observed at the presumed substrate-binding cavities

173    of FLVCR1 and FLVCR2, respectively. This chemical environment is found analogously in the prokaryotic

174    choline transporter LicB, as well as predicted models of eukaryotic choline transporters[19–21] (Extended

175    Data Fig. 6). Indeed, we obtained cryo-EM maps of choline-bound structures of FLVCR1 and FLVCR2 at

176    a resolution of 2.6 Å and 2.8 Å, respectively (Fig. 3d,e and Extended Data Fig. 2b and 3c). Both structures

177    were captured in the inward-facing conformation, suggesting that choline is also capable of resolving

178    the conformational heterogeneity in FLVCR2 by trapping it in an inward-facing substrate-bound state.

179    Intriguingly, this effect is opposite to that of heme described above. The choline-bound structures

180    exhibit a C$\alpha$ r.m.s.d. of 0.688 Å (FLVCR1) and 1.002 Å (FLVCR2) to their respective apo inward-facing

181    structures. The choline-bound inward-facing structures of FLVCR1 and FLVCR2 resemble each other and

182    their substrate binding sites are found in analogous locations within the transporter scaffold. The

183    bound choline molecule is caged inside the central binding site between the two domains of the FLVCRs,

184    surrounded mainly by TMs 1, 2, 4, 5, 7, and 11 (Fig. 3d,e). The binding sites in the two transporters are

185    formed by a suite of conserved residues. The central coordinating tryptophan residue (W102[FLVCR1] and

186  W125$^{FLVCR2}$) of TM1 is located above the choline, constraining the diffusion of the molecule towards the

187  external gate. Two additional aromatic residues of TM7, one tyrosine (Y325 $^{FLVCR1}$ and Y349$^{FLVCR2}$) and

188  one phenylalanine (F348$^{FLVCR1}$ and F324$^{FLVCR2}$), line the peripheral space of the binding site and restrict

189  the movement of the choline within the pocket. Our MD simulations demonstrate that the quaternary

190  ammonium group of choline stably interacts with the conserved tryptophan residue (W125$^{FLVCR1}$ and

191  W102$^{FLVCR2}$), forming concomitant cation-$\pi$ interactions with both the tryptophan and tyrosine residues

192  (Fig. 3f,g). The hydroxyl group of the choline molecule showed more versatile interactions. Two

193  asparagine residues identified near the hydroxyl group formed transient hydrogen bonds with choline

194  during our simulations. In addition, at least two interacting water molecules were consistently present

195  near the OH-group of the bound choline, which was predominantly oriented away from the conserved

196  tryptophan towards the solvent phase (Supplementary Fig. 4 and Supplementary Video 3). It is

197  noteworthy that all these coordinating residues are fully conserved in mammals, suggesting a

198  specialized role of FLVCRs in recognizing and transporting choline across species (Fig. 3h).

199

200  To gain further insights into the spectrum of substrate selectivity of FLVCR1 and FLVCR2, we performed

201  nano differential scanning fluorimetry (nanoDSF) using choline, phosphocholine, and betaine as

202  candidate substrates (Fig. 3i and Extended Data Fig. 7). For both transporters, strong quenching of

203  tryptophan fluorescence could be observed by the addition of choline, but not its structurally related

204  metabolites (Fig. 3i). We determined choline dissociation rate constants for FLVCR1 at 25.10 ± 1.26 $\mu$M

205  and FLVCR2 at 125.22 ± 4.87 $\mu$M[22]. Subsequently, we attempted to assess the kinetic properties of both

206  FLVCRs via a solid-supported membrane-based electrophysiological (SSME) approach (Fig. 3j). For both

207  transporters we observed a rapid increase in current upon application of choline, followed by a fast

208  current decay, which can be attributed to an electrogenic substrate binding induced pre-steady state

209  (PSS) event. However, only for FLVCR2, a second current phase was observed, revealing a much slower

210  decay time constant. This current phase is typical for transport events that slowly charge the membrane

211  capacitor in SSME experiments[23,24]. Despite the structural similarities described above, FLVCRs seem to

212  have different kinetic fingerprints that might either originate from subtle structural differences

213    identified at the termini of the two transporters, or specific requirements to their surrounding

214    environment. Further, our data indicate that FLVCR-facilitated choline transport displays no immediate

215    pH dependency within the physiological range tested in our assay (Extended Data Fig. 8). Thus, we

216    conclude that FLVCRs most likely represent choline-driven uniporters. We then determined choline

217    binding affinities based on the PSS peaks and obtained values of 0.52 ± 0.07 mM for FLVCR1 and 3.28

218    ± 0.31 mM for FLVCR2. While the absolute affinities deduced from the SSME experiments are weaker

219    than those from the more direct DSF measurements, which may reflect an underlying transport phase,

220    the relative values consistently demonstrate a similar 5- to 6-fold difference in choline affinity between

221    the two transporters[25]. We note that our DSF-derived binding affinities more likely reflect values that

222    are realistic in a biological setting, as plasma choline concentrations are relatively stable at 5-10 μM[26].

223 *Translocation pathway of choline in FLVCRs*

224 MFS transporters typically cycle between inward- and outward-facing conformations, facilitating

225 substrate translocation in an alternating-access manner. Substrate binding often plays a pivotal role in

226 eliciting the conformational transitions[27]. Our cryo-EM data support this mechanism for at least FLVCR2,

227 where we see a full transition from the outward-facing to inward-facing state upon choline binding.

228 Our MD simulations map the route for substrate entry along the pathway in the outward-facing

229 conformation of FLVCR2. After spontaneously diffusing into the opening, choline initially interacts with

230 several residues near the protein surface, mainly D124 (Supplementary Fig. 5). It sequentially

231 approaches the deeper recesses of the cavity, primarily engaging with conserved aromatic residues

232 W102 and Y325. In a particular entry event, we observed choline moving to a position below the W102

233 residue within the binding site, consistent with our observations in the choline-bound structure of

234 FLVCR2 (Supplementary Video 4).

235

236 The substantial global conformational changes triggered by choline further alter the local arrangement

237 of substrate-coordinating residues within the translocation pathway. The rearrangement of the binding

238 site results in a more constricted pocket, promoted by the inward movement of the conserved residues

239 closer to the choline molecule (Extended Data Fig. 9a). The repositioning of these residues, especially

240 of the aromatic side chains, restricts the accessibility of the binding pocket and promotes choline

241 capture and engulfment.

242

243 The choline-bound inward-facing conformations likely represent the pre-release phase during the

244 translocation. In their choline-bound structures, the cavities of both FLVCRs share common

245 characteristics, exhibiting a neutral interior but a negatively charged surface at the exit (Extended Data

246 Fig. 5b,e). FLVCR1 features a slightly smaller cavity volume of 513 $Å^3$ compared to 579 $Å^3$ of FLVCR2

247 (Extended Data Fig. 9b). In an inter-domain interaction site at the cavity opening, a serine residue of

248 TM4 (S222[FLVCR1] and S199[FLVCR2]) and a glutamate side chain of TM11 (E459[FLVCR1] and E435[FLVCR2]) remain

249 in close proximity even with the internal gate open (Extended Data Fig. 9c,d). While these conserved

250    residues may interact to limit pathway accessibility, a peripheral solvent-accessible channel emerging

251    from the internal space to the binding site reveals a semi-open translocation pathway in the choline-

252    bound inward-facing conformations of both transporters (Extended Data Fig. 9b).

253

254    In our MD simulations, we captured a spontaneous choline release event from FLVCR2 through the

255    semi-open pathway that would complete the translocation process (Supplementary Video 5). The

256    choline spontaneously left the binding site after ~700 ns, transited in steps through the half channel,

257    and then escaped into the solvent at ~900 ns. Our apo inward-facing structures plausibly illustrate the

258    following post-release states. We speculate that an event occurs during the substrate release process

259    in both FLVCRs, resulting in the dissipation of the conserved serine-glutamate interactions and causing

260    the full opening of the internal cavity. This is suggested by our observations that the distance between

261    the S-E residues expands in the apo inward-facing structures relative to the choline-bound states

262    ($\Delta d_{FLVCR1}$ = 3.3 Å and $\Delta d_{FLVCR2}$ = 5.2 Å; Fig. 2e, Extended Data Fig. 4d and 9c,d). A subtle conformational

263    transition takes place upon the release of the choline in both FLVCRs, manifested by a rigid-body shift

264    between two domains that moves the inner halves slightly away from the central axis perpendicular to

265    the membrane plane (Extended Data Fig. 9e,f). The rearrangement of the TMs results an increased

266    angle between the N-domain and C-domain, widening by 0.9° in FLVCR1 compared to 4.3° in FLVCR2.

267    Consequently, the central cavities become less compact, enlarging from volumes of 513 $Å^3$ and 579 $Å^3$

268    for FLVCR1 and FLVCR2, to 771 $Å^3$ and 1046 $Å^3$, respectively. Meanwhile, the molecular architecture of

269    the external gate remains largely unchanged in the post-release inward-facing states of both FLVCRs

270    (Fig. 2d, Extended Data Fig. 4c and 9c).

271

272    Choline binding and release events drive additional local rearrangements in the translocation pathway

273    of FLVCR2. The inward-facing apo structure of FLVCR2 reveals a distinct lateral opening of the pathway,

274    directed towards the inner membrane leaflet of the lipid bilayer (Extended Data Fig. 10). This channel,

275    located between TM5 (N-domain) and TM8 (C-domain), accommodates a lipid/detergent-like density

276    in the apo state, as observed in our cryo-EM results (Extended Data Fig. 10b). Yet, when choline is

277    present in the central cavity, residue F220 seals the opening and prevents the lipid/detergent-like

278    density from accessing the channel (Extended Data Fig. 10c). The relevance of this site for

279    environmental interactions was further supported during our simulations with FLVCR2, where lipid-

280    entering events were observed (Extended Data Fig. 10a). The displacement of F220 allowed one of the

281    lipid's acyl tails to enter and reside within this channel. Whether or not this might be connected to a

282    putative allosteric regulatory mechanism linked to lipid binding in FLVCR2 as observed in other MFS-

283    type transporters remains to be further investigated[28,29].

284 **Discussion**

285 FLVCR transporters were considered to be human heme transporters. In this study, we have determined

286 cryo-EM structures of FLVCR1 and FLVCR2 in distinct apo, heme and choline-bound states, providing

287 valuable insights into architecture, substrate interaction and conformational dynamics of these two

288 MFS transporters. Our data support previous studies regarding the heme-binding properties of FLVCR2,

289 yet clearly demonstrate that choline is the transport substrate of both FLVCRs. Based on our structural

290 findings, we suggest a rocker-switch alternating-access mechanism for the transport cycle of choline

291 import (Fig. 4). As the resting state, the apo outward-facing FLVCR2 conformation is set up for choline

292 binding from the external space. Substrate-induced conformational changes drive FLVCR2 towards its

293 inward-facing state. Finally, the choline will be released to the cytosol or the mitochondrial matrix,

294 depending on the sub-cellular localization of FLVCR1 and FLVCR2[18]. Subsequent to choline release,

295 FLVCRs will transition into their outward-facing state in order to re-initiate the transport cycle. Our

296 structural data did not reveal fully occluded conformations that are key features of alternating access.

297 Hence, we suspect that these occluded conformations exist only transiently and rapidly convert

298 towards either the inward- or outward-facing conformations.

299

300 Our findings suggest that FLVCRs act as uniporters, conducting facilitated diffusion across the

301 membrane. Uniporters conventionally utilize the chemical potential of substrates as the only energy

302 source driving the transport process thermodynamically[30]. This mechanism appears to match the

303 kinetic fingerprints of FLVCRs observed in the SSM-based assays. Our cryo-EM data also reveal that

304 choline-binding prompts the conformational transition in FLVCR2 from the outward-facing to the

305 inward-facing state without requiring additional energy inputs. Corroborating this finding, our MD

306 simulation of FLVCR2 captured several spontaneous entry events of choline into the cavity in the

307 outward-facing conformation, including a traverse below the central coordinating tryptophan residue,

308 reminiscent of the local binding environment in the inward-facing choline-bound state (Supplementary

309 Fig. 5 and Supplementary Video 4). Furthermore, we observed a release event of choline from the

310 inward-facing conformation of FLVCR2 (Supplementary Video 5).

311

312    While choline is the primary transport substrate for FLVCR2, it should be highlighted that heme can

313    also induce conformational changes, albeit leading to the opposing outward-facing state. This concurs

314    with the previous reports that FLVCR2 is capable of binding heme with the N-domain yet not

315    transporting it[16,18,31]. As labile cytoplasmic heme is readily degraded by heme oxygenase, we anticipate

316    that the heme interaction of FLVCR2 will be restricted to mitochondria where heme biogenesis takes

317    place. We performed matrix targeting sequences (MTSs) predictions to identify the targeting sequence

318    of FLVCR2[32]. The N-terminal region of FLVCR2 exhibits a propensity score comparable to that of proteins

319    known to be trafficked to the mitochondria (Supplementary Fig. 6). Correspondingly, the endogenous

320    FLVCR2 protein, originating from its chromosomal locus, has been previously reported to localize within

321    mitochondria[18]. We conclude that the physiological role of FLVCR2 is most likely to act as a

322    mitochondrial choline importer that may be regulated by the availability of heme within the

323    mitochondrial matrix. In addition, our MD simulations revealed that a physiological mitochondrial

324    membrane potential influences the rates of choline entry and release in FLVCR2, favoring inward-

325    directed translocation of this positively charged substrate (Supplementary Fig. 7 and Supplementary

326    Table 1). Choline import in rat kidney mitochondria was previously found to depend on the membrane

327    potential, which matches with our observations[33]. In contrast to FLVCR2, FLVCR1 showed no binding or

328    response to heme, and obtained a very low propensity score in the MTSs prediction (Supplementary

329    Fig. 6). Combined with insights from genome-wide association study data, we presume that FLVCR1

330    acts as a plasma membrane-localized choline transporter[34].

331

332    The successful elucidations of FLVCR structures in their choline-bound state establish the SLC49 family

333    as a new class of human choline transporters[20]. Despite the positive charge of choline, the fully

334    conserved binding site in FLVCRs exhibits a neutral charge environment. As a result, the coordination

335    of bound choline is predominantly mediated by the cation-$\pi$ interaction formed between the

336    trimethylammonium group of choline and conserved aromatic residues. In a similar manner, the

337    bacterial choline transporter LicB features a binding site composed of six aromatic and one amide side

338  chains, including W17 of TM1 that corresponds to the critical coordinating tryptophan residues in

339  FLVCRs[19] (Extended Data Fig. 6a). We performed a comparative analysis using the AlphaFold2 structures

340  of other putative human choline transporters (Extended Data Fig. 6b-d). Our examination of these

341  structures reveals binding pockets containing aromatic residues. In the high-affinity choline transporter

342  SLC5A7, the putative binding pocket encompasses four tryptophan and two tyrosine residues,

343  potentially forming a cation-π trap. The CTL (SLC44) family members feature a unique fold and the exact

344  position of their binding site remains unclear due to the absence of high-resolution structures. However,

345  the putative pocket of human SLC44A1 suggests the involvement of a tyrosine residue in choline

346  coordination[35]. The SLC22 family members share the same MFS fold with FLVCRs, and their putative

347  binding site with a broad substrate spectrum also contains aromatic and amide side chains that are

348  potential participants in choline coordination[36]. Our structural findings and analyses suggest that

349  cation-π interactions may be a common principle for choline coordination. While the cation-π

350  interaction appears to be highly specific and selective for substrate coordination in FLVCRs, our data

351  suggest that the hydroxyl group of choline preferentially forms promiscuous and dynamic interactions

352  either with the surrounding protein environment, such as amide-containing residues, or with water

353  molecules.

354

355  Choline, an indispensable quaternary ammonium cation with water-soluble vitamin-like characteristics,

356  is vital for a myriad of biological processes[37]. Dietary choline uptake mediated by certain transporters

357  is necessary as our bodies have limited capacity for *de novo* synthesis[38]. Choline deficiency is linked to

358  a plethora of undesired health consequences, for instance, skeletal muscle atrophy and

359  neurodegenerative diseases[39]. Additionally, abnormal choline metabolism is emerging as a hallmark for

360  oncogenesis and pathological inflammatory conditions[20,40,41]. Disorders including PCARP and DBA

361  associated with FLVCR1 and the Fowler syndrome related to FLVCR2 might stem from choline deficiency

362  that leads to developmental or degenerative complications. In conjunction with the known

363  physiological importance of choline and our current findings, a link between defective FLVCR function

364  and the associated pathologies becomes evident. Choline stands as the precursor for essential

365     compounds, such as the membrane phospholipid phosphatidylcholine (PC), the neurotransmitter

366     acetylcholine, and the methyl group donor betaine[39]. Altered choline metabolism is apt to cause

367     abnormal cell proliferation and differentiation conditions, impacting especially the nervous and

368     hematologic systems due to disturbances in neurotransmitter synthesis and methylation activities[42,43].

369     Beyond these impacts, choline metabolism in macrophages also affects mitochondrial morphology and

370     metabolism[41]. The disruption of PC synthesis results in the destruction of mitochondrial cristae,

371     compelling cells to rely only on substrate-level phosphorylation for ATP production. A handful of animal

372     studies have further underscored the interplay between choline supplementation and brain

373     development, particularly in angiogenesis[44–47]. Choline deficiency has been linked to decreased DNA

374     methylation within the promoters of genes that are important regulators of angiogenesis[44]. Moreover,

375     dysfunctional mutations or complete loss of choline transporters SLC5A7 or SLC44A1 have been

376     implicated in certain neurodegenerative conditions, including but not limited to distal hereditary motor

377     neuronopathy, congenital myasthenic syndrome, and childhood-onset neurodegeneration[48–52]. The

378     precise molecular mechanisms linking choline transport to these disorders are not yet fully deciphered

379     and require further study given their clinical implications.

380 **Online Methods**

381

382 **Generation of Inducible HEK293 Stable Cell Lines.**

383 The complementary DNAs of full-length wildtype FLVCR1 (human SLC49A1, NCBI Reference Sequence

384 NM_014053) and FLVCR2 (human SLC49A2, NCBI Reference Sequence: NM_017791) were cloned into

385 pcDNA5/FRT/TO (Invitrogen) vectors, respectively. The gene for both FLVCRs was modified by a C-

386 terminal FLAG fusion tag. Further details are found in sequence data provided as supplementary

387 information (Supplementary Tables 2 and 3). The recombinant Flp-In T-REx293-FLVCR1 and Flp-In T-

388 REx293-FLVCR2 cell lines were generated by using a tetracycline-inducible and commercially available

389 Flp-In T-REx host-cell line system from Invitrogen. Flp-In T-REx293 cells were cultured in high-glucose

390 Dulbecco's Modified Eagle's Medium (DMEM; Sigma-Aldrich) supplemented with 10% fetal bovine

391 serum (FBS; Gibco), 1% Pen/Strep (Gibco), 1 $\mu$g ml$^{-1}$ Zeocin (Thermo Fisher), and 15 $\mu$g ml$^{-1}$ blasticidin

392 S hydrochloride (AppliChem) at 37 °C in an atmosphere of 5% $CO_2$. Cells were not tested for

393 mycoplasma contamination. For stable integration, the pcDNA5/FRT-FLVCR1-FLAG and pcDNA5/FRT-

394 FLVCR2-FLAG vectors were cotransfected with the Flp recombinase encoding expression vector pOG44

395 (Thermo Fisher) at a 1:13 mass ratio, respectively. All transfection procedures were performed with

396 Lipofectamine™ 2000 reagent according to the manufacturer's instructions (Thermo Fisher). To select

397 stable clones, transfected cells were cultivated with growth medium containing 100 $\mu$g ml$^{-1}$ hygromycin

398 B (AppliChem).

399

400 **Production and Purification of the human FLVCR1 and FLVCR2.**

401 For protein production, the Flp-In T-REx293-FLVCR1 and Flp-In T-REx293-FLVCR2 cell lines were cultured

402 in roller bottles (Greiner Bio-One) in growth media containing 100 $\mu$g ml$^{-1}$ hygromycin B for 14 d under

403 the above-mentioned conditions. Gene expression was induced at 100% confluence by adding a final

404 concentration of 2 $\mu$g ml$^{-1}$ doxycycline hydrochloride. After 72 h, cells were harvested with Accutase

405 solution (Sigma-Aldrich) and stored at −80 °C until further use. Harvested cells were suspended in cold

406 lysis buffer containing 25 mM Tris pH 7.4, 150 mM NaCl, and 0.1 g ml$^{-1}$ SigmaFast

407     ethylenediaminetetraacetic acid (EDTA)-free protease inhibitor (Sigma-Aldrich) and disrupted by

408     stirring under high-pressure nitrogen atmosphere (750 MPa) for 45 min at 4 °C in a cell-disruption

409     vessel (Parr Instrument). The cell lysate was centrifuged at 8,000$g$ at 4 °C for 15 min. Subsequently, the

410     low-velocity supernatant was centrifuged at 220,000$g$ at 4 °C for 60 min. Pelleted membranes were

411     resuspended and stored in a storage buffer containing 25 mM Tris pH 7.4, 150 mM NaCl, 10% glycerol

412     (v/v), and 0.1 g ml$^{-1}$ SigmaFast EDTA-free protease inhibitor (Sigma-Aldrich).

413

414     All purification steps of both FLVCRs were performed at 4 °C. Isolated membranes were solubilized with

415     1% (w/v) lauryl maltose neopentyl glycol (LMNG; GLYCON Biochemicals) with gentle stirring for 1 h.

416     The insoluble membrane fraction was removed via ultracentrifugation at 220,000$g$ for 1 h.

417     Subsequently, the supernatant was incubated with ANTI-FLAG® M2 Affinity Gel resin (Merck) for 1 h.

418     The resin was preequilibrated with a buffer containing 50 mM Tris pH 7.4, 150 mM NaCl, and 0.02%

419     LMNG (w/v). The washing step was performed using 20 column volumes (CVs) of wash buffer [50 mM

420     Tris pH 7.4, 150 mM NaCl, 5% (v/v) glycerol, and 0.02% LMNG). The protein was eluted from the M2

421     resin with 10 CVs of the same buffer supplemented with 4 mM FLAG® Peptide (Merck). The eluted

422     sample was concentrated and subjected to a Superdex 200 Increase 10/300 column (GE Healthcare)

423     equilibrated with size exclusion chromatography (SEC) buffer [50 mM Tris pH 7.4, 150 mM NaCl, and

424     0.001% (w/v) LMNG]. Peak fractions were pooled, concentrated to 1.5 mg ml$^{-1}$ using an Amicon 50-kDa

425     cut-off concentrator (Merck Millipore), and stored for further analysis.

426

427     For the dodecyl maltoside (DDM) and cholesterol hemisuccinate (CHS) solubilized samples used for

428     proteoliposome reconstitution, the proteins were purified based on the same protocol. The membrane

429     solubilization buffer contains 1% (w/v) DDM/0.2% (w/v) CHS instead of LMNG. Similarly, the wash

430     buffer contains 0.1% (w/v) DDM/0.02% (w/v) CHS, and the SEC buffer contains 0.02% (w/v) DDM/0.004%

431     (w/v) CHS.

432

433     **Immunoblotting**

434    Affinity-purified proteins were subjected to SDS-PAGE and immunoblotting. FLAG-tagged FLVCR1 and

435    FLVCR2 were detected using anti-FLAG (F3165, Sigma-Aldrich) antibodies at 1:1,000 dilution. Anti-

436    mouse IgG antibody conjugated with alkaline phosphatase (A9316, Sigma-Aldrich) was used as

437    secondary antibody at 1:5,000 dilution.

438

439    **Nano differential scanning fluorimetry (nanoDSF)**

440    NanoDSF measurements were carried out using Prometheus Panta (NanoTemper Technologies).

441    Purified protein samples were diluted with DSF buffer containing 50 mM HEPES pH 7.4, 150 mM NaCl,

442    and 0.001% (w/v) LMNG to 1 $\mu$M. Buffers with different concentrations of choline, phosphocholine, or

443    betaine were prepared by serial dilutions of DSF buffer containing 4 mM of the compounds. The protein

444    samples were mixed with an equal volume of DSF buffer or the compound-containing buffer with a

445    final protein concentration of 0.5 $\mu$M and then incubated at room temperature for 15 min. A volume

446    of 10 µl mixed solution was used per Prometheus high sensitivity capillary (NanoTemper Technologies).

447    A temperature ramp of 1 °C min$^{-1}$ from 25 to 95 °C was applied while the intrinsic protein fluorescence

448    at 330 and 350 nm was recorded. Analysis of the initial ratio of $F_{350}/F_{330}$ was carried out using Python

449    libraries including pandas, numpy, scipy and seaborn in Visual Studio Code (Microsoft). Three technical

450    replicates were recorded for data analysis.

451

452    **Proteoliposome preparation**

453    1-palmitoyl-2-oleoyl-sn-glycero-3-phosphoethanolamine (POPE, Avanti) and 1-Palmitoyl-2-oleoyl-*sn*-

454    glycero-3-phospho-(1'-rac-glycerol) (POPG, Avanti) in chloroform (25mg ml$^{-1}$) were mixed at the ratio

455    of 3:1 (w/w), followed by gentle evaporation of the chloroform and overnight desiccation under a

456    stream of nitrogen gas. The dried lipids were suspended in internal buffer comprised of 50 mM HEPES

457    pH 7.4, 150 mM NaCl to a final concentration of 12.5 mg ml$^{-1}$ and sonicated until homogenous. The

458    lipid solution was subjected to three freeze-thaw cycles and extruded through a 400-nm polycarbonate

459    filter (Avestin) to generate unilamellar vesicles. The liposomes were destabilized by the addition of 0.13%

460    (w/v) Triton-X100 (Sigma) at room temperature. Purified DDM/CHS-solubilized FLVCR1 or FLVCR2

461    samples was added at a 1:50 protein-to-lipid mass ratio and incubated for 15 min at 4 °C. Protein-free

462    liposomes were prepared in parallel using the same concentration of DDM/CHS. The detergent was

463    removed by several additions of SM2-BioBeads (Bio-Rad). Firstly, 0.05 g ml$^{-1}$ of BioBeads were added

464    to the sample and incubated with gentle agitation for 1 h at 4 °C, then 0.05 g ml$^{-1}$ BioBeads were added

465    followed by incubation overnight at 4 °C, and finally 0.08 g ml$^{-1}$ BioBeads were added with 2-h

466    incubation at 4 °C. BioBeads were removed by filtration and liposomes were collected by

467    ultracentrifugation at 264,000$g$ for 20 min and resuspended at a concentration of 8 mg ml$^{-1}$ lipids in

468    internal buffer. The reconstituted liposomes were flash frozen in liquid nitrogen and stored at −80 °C.

469

470    **SSM-based electrophysiology (SSME) assays**

471    SSM-based electrophysiology was performed on a SURFE$^2$R N1[53] (Nanion Technologies). For all

472    experiments, preparation of 3-mm sensors was performed as described[54]. For measurements, a single

473    solution exchange configuration was employed that consisted of three phases of 0.5 s duration each:

474    flow of non-activating solution (NA), activating solution (A), and non-activating solution (NA). Both NA

475    and A were prepared from the same main buffer (30 mM HEPES, 30 mM MES, and 300 mM NaCl at pH

476    7.4), while A was supplemented with choline chloride and NA was prepared by adding NaCl in an

477    equimolar manner. For the choline dose response curve, 50 mM choline chloride and 50 mM NaCl were

478    used to achieve A0 and NA (with the highest salt concentration), followed by dilution of A0 using NA

479    to generate all A solutions with choline concentrations ranging between 50 to 0.02 mM choline, while

480    keeping the total osmolarity constant. Proteoliposomes or liposomes (negative control) were thawed

481    and diluted 1:5 in NA, and sonicated using a bath sonicator for 20 s. A volume of 10 μl of the diluted

482    proteoliposomes were added to the sensors, and then centrifuged at 2,000$g$ for 30 min. Assays were

483    performed on both sample and negative control to distinguish currents originating from FLVCRs and

484    artifact currents induced by the choline$^+$/Na$^+$ exchange due to interactions of the ions with the

485    membrane surface. Currents corresponding to different substrate concentrations were measured on

486    the same sensor, with a total of four different sensors. To determine transport kinetics of choline for

487    each FLVCR transporter, the measured currents for a given substrate concentration had the average

488    value of the corresponding negative control current subtracted from it. For the measurement at

489    different pH conditions, again the single solution exchange configuration was used. The main buffer

490    was titrated to different pH values that are physiologically relevant, ranging between 6 and 8, before

491    splitting into A supplemented with 15 mM choline chloride and the corresponding NA supplemented

492    with 15 mM NaCl. Before each measurement at a given pH, the pH was equilibrated via incubation for

493    3 minutes in NA solution at the given pH. Subsequently, peak currents were measured upon the

494    addition of A at the same pH. All pH values were measured sequentially using the same sensor, with a

495    total of four sensors. For both dose response curves and pH measurements, the error bars represent

496    the s.d. As the peak current signal can be a combined effect of electrogenic PSS and transport events[24],

497    we use the $EC_{50}$ parameter to describe the concentration that generates the half maximum response.

498    Analysis of the data was performed in OriginPro (OriginLab Corporation).

499

500    **Cryo-EM sample preparation**

501    In order to collect cryo-EM data of FLVCR1 and FLVCR2 in different sample conditions, different

502    combinations of FLVCR proteins and putative substrate molecules were prepared. For both as-isolated

503    samples of FLVCRs, the protein concentration was adjusted to approximately 1.5 mg ml$^{-1}$ and subjected

504    to plunge freezing. For samples supplemented with heme, heme loading was performed prior to the

505    SEC during protein purification with a 10-fold molar excess to the protein concentration. Peak fractions

506    were pooled and concentrated to 1.5 mg ml$^{-1}$ before sample vitrification. For samples supplemented

507    with choline, purified proteins were adjusted to 1.5 mg ml$^{-1}$ and choline was added at a final

508    concentration of 1 mM. The samples were incubated for 10 minutes at room temperature before

509    plunge freezing. Identical plunge freezing conditions were applied for all samples: Quantifoil R1.2/1.3

510    copper grids (mesh 300) were washed in chloroform and subsequently glow-discharged with a PELCO

511    easiGlow device at 15 mA for 90 seconds. A volume of 4 µl sample was applied to a grid and blotting

512    was performed for 4 seconds at 4 °C, 100% humidity with nominal blot force 20 immediately before

513    freezing in liquid ethane, using a Vitrobot Mark IV device (Thermo Scientific).

514

**Cryo-EM image recording**

515

516    For each cryo-EM sample, a dataset was recorded in Energy-Filtered Transmission Electron Microscopy

517    (EF-TEM) mode using either a Titan Krios G3i or a Krios G4 microscope (Thermo Scientific), both

518    operated at 300 kV. Electron-optical alignments were adjusted with EPU 3.0 - 3.4 (Thermo Scientific).

519    Images were recorded using automation strategies of EPU 3.0 - 3.4 in electron counting mode with

520    either a Gatan K3 (installed on Krios G3i) or a Falcon4 (installed on Krios G4) direct electron detector.

521    For Gatan K3 detector, a nominal magnification of 105,000, corresponding to a calibrated pixel size of

522    0.837 Å was applied, and dose fractionated movies (80 frames) were recorded at an electron flux of

523    approximately 15 $e^-$ x pixel$^{-1}$ x s$^{-1}$ for 4 s, corresponding to a total dose of ~80 $e^-$/A$^2$. For Falcon4 detector,

524    a nominal magnification of 215,000, corresponding to a calibrated pixel size 0.573 Å was applied, dose

525    fractionated movies were recorded in electron-event representation (EER) format at an electron flux

526    of approximately 4 $e^-$ x pixel$^{-1}$ x s$^{-1}$ for 5 s, corresponding to a total dose of ~50 $e^-$/A$^2$. Images were

527    recorded between -1.1 and -2.0 μm nominal defocus. Data collection quality was monitored through

528    EPU v. 3.0-3.4 and CryoSparc Live (versions 3.0 and 4.0)[55].

529

**Cryo-EM image processing**

530

531    For each acquired dataset, the same cryo-EM image processing approach was applied: MotionCor2 was

532    used to correct for beam-induced motion and to generate dose-weighted images[56]. Gctf was used to

533    determine the contrast transfer function (CTF) parameters and perform correction steps[57]. Images with

534    estimated poor resolution (>4 Å) and severe astigmatism (>400 Å) were removed at this step. Particles

535    were picked by TOPAZ and used for all further processing steps[58]. 2D classification, initial model

536    generation, 3D classification, CTF refinement, Bayesian polishing, 3D sorting, and final map

537    reconstructions were performed using RELION (versions 3.1 and 4.0) or cryoSPARC (versions 3.0 and

538    4.0)[55,59,60]. Fourier shell correlation (FSC) curves and local-resolution estimation were generated in

539    RELION or cryoSPARC for individual final maps. A schematic overview of our processing workflow, and

540    a summary of map qualities are shown in Extended Data Figs. 1-3, and Supplementary Table 4.

541

**542 Model building and geometry refinement**

543 The first atomic model of FLVCR1 and FLVCR2 were built into the respective EM density maps of the as-

544 isolated state in Coot (version 0.8) or ISOLDE within ChimeraX (version 1.5 and 1.6)[61–63], using the

545 AlphaFold predicted structures as initial templates[21]. After manual backbone tracing and docking of

546 side chains, real-space refinement in Phenix was performed (version 1.18)[64]. Refinement results were

547 manually inspected and corrected if required. This model was used as a template to build all

548 subsequent atomic models. The finalized models were validated by MolProbity implemented in

549 Phenix[65]. Map-to-model cross-validation was performed in Phenix (version 1.18). $FSC_{0.5}$ was used as

550 cut-off to define resolution. A summary of model parameters and the corresponding cryo-EM map

551 statistics is found in Supplementary Table 4. The finalized models were visualized using ChimeraX. The

552 built models of both FLVCR proteins in different states were used as starting structures for MD

553 simulations.

554

**555 Molecular dynamics simulations**

556 All simulations were run using GROMACS 2022.4[66]. The protein structures were embedded in a lipid

557 bilayer with 75% POPE and 25% POPG with CHARMM-GUI[67] and solvated in TIP3P water with 150 mM

558 NaCl. The charmm36m force field[68] was used with the improved WYF parameter set for cation-pi

559 interactions[69]. Initial systems were minimized for 5000 steepest descend steps and equilibrated for 450

560 ps of MD in an NVT ensemble and for 1.5 ns in an NPT ensemble. Position restraints of 4000 and 2000

561 kJ $mol^{-1}$ $nm^{-2}$ in the backbone and side chain heavy atoms, respectively, were gradually released during

562 equilibration. The z-positions of membrane phosphates, as well as lipid dihedrals, were initially

563 restrained with force constants of 1000 kJ $mol^{-1}$ $nm^{-2}$ and 1000 kJ $mol^{-1}$ $rad^{-2}$, respectively, which were

564 gradually released during equilibration. The initial time step of 1 fs was increased to 2 fs during NPT

565 equilibration. Long range electrostatic interactions were treated with particle-mesh Ewald (PME) with

566 a cut-off of 1.2 nm[70]. Van-der-Waals interactions were cut off beyond a distance of 1.2 nm. The LINCS

567 algorithm was used to constrain the bonds involving hydrogen atoms[71]. During equilibration, a constant

568 temperature of 310 K was maintained with the Berendsen thermostat, using a coupling constant of 1

569  ps[72]. Constant pressure of 1 bar was established with a semi-isotropic Berendsen barostat and a

570  coupling constant of 5 ps. In the production runs, a Nosé–Hoover thermostat and a Parrinello–Rahman

571  barostat were used[73,74].

572

573  We used our cryo-EM structures as initial models for simulations of apo and choline-bound inward-

574  facing FLVCR1, apo and choline-bound inward-facing FLVCR2, and apo outward-facing FLVCR2. An initial

575  structure of choline-bound outward-facing FLVCR2 was generated aligning apo outward-facing FLVCR2

576  to choline-bound inward-facing FLVCR2 and maintaining choline in the cavity. In choline entry

577  simulations, the apo structures were used with 380 mM choline in solution. Simulations of heme-

578  bound outward- and inward-facing FLVCR2 were prepared by manually placing heme close to the

579  observed binding region in the N-terminus of the apo structures, outside of the lipid bilayer.

580  Additionally, a simulation of FLVCR2 in the outward-facing conformation was conducted, with the heme

581  initially positioned in front of the cavity entrance. Three replicas with random initial velocities from the

582  Boltzmann distribution were run for the rest of the systems. Choline release simulations were

583  interrupted after choline exit from the cavity, and hence have variable duration. For all other systems,

584  each replica was run for 1 μs. To reproduce mitochondrial membrane potential, an additional set of

585  simulations was run for choline-bound inward- and outward-facing, and apo outward-facing FLVCR2

586  with choline in solution, in which an electric field of -200 mV was applied in the z-dimension.

587

588  Visual Molecular Dynamics (VMD) and MDAnalysis were used to visualize and analyze the trajectories,

589  respectively[75,76].

590

591  **Interior tunnels and cavities**

592  Tunnels and cavities were mapped with MOLE 2.5 with a bottleneck radius of 1.2 Å, bottleneck

593  tolerance 3 Å, origin radius 5 Å, surface radius 10 Å, probe radius 5 Å and an interior threshold of 1.1 Å[77].

594

595    We calculated the volume of the cavity using CASTp with a bottleneck radius of 1.4 Å. Residues 297-

596    320 and 512-516 were removed from the FLVCR1 model to avoid the misattribution of the volume

597    between internal loops to the cavity volume[78]. Analogously, residues 272-296 and 487-502 were not

598    included in the cavity volume calculation of FLVCR2.

599

600    **Multiple sequence alignments**

601    Multiple sequence alignments of FLVCR1 and FLVCR2 from *homo sapiens*, *Felis catus*, *Mus musculus*,

602    and *Sus scrofa* were performed using Clustal Omega[79].

**Data availability**

Cryo-EM maps are deposited at the Electron Microscopy Data Bank under accession numbers: EMD-18334, EMD-18335, EMD-18336, EMD-18337, EMD-18338, EMD-18339. Atomic models of human FLVCR1 and FLVCR2 have been deposited to the Protein Data Bank under accession numbers: 8QCS, 8QCT, 8QCX, 8QCY, 8QCZ, 8QD0. All other data is presented in the main text or supplementary materials. Source data are provided with this paper.

**Author contributions**

T-H.W. purified proteins, performed biochemical assays, prepared grids, collected cryo-EM data, processed cryo-EM data, refined the structure, built the model, co-drafted the manuscript, and prepared figures. A.C.C. performed MD simulations, analyzed data, co-drafted the manuscript, and prepared figures. W.J. performed cell productions, optimized purification conditions, and purified proteins. A.B. performed SSM-based assays, analyzed data, and prepared figures. S.W. calibrated and aligned the microscope. G.G. assisted in cell culturing and protein purification. G.H., D.W., and S.S. supervised the project. D.W. implemented cell production and protein purification, prepared grids, performed initial cryo-EM screening experiments, collected cryo-EM data, analyzed data, drafted the manuscript, and funded the project. D.W. and S.S. initiated the project. S.S. designed research, evaluated data, funded the project, drafted the manuscript, and generated figures.

**Competing interests**

The authors declare no conflict-of-interest.

634 **References**

635 1. Khan, A. A. & Quigley, J. G. Heme and FLVCR-related transporter families SLC48 and SLC49. *Mol.*

636 *Asp. Med.* **34**, 669–682 (2013).

637 2. Tailor, C. S., Willett, B. J. & Kabat, D. A putative cell surface receptor for anemia-inducing feline

638 leukemia virus subgroup C is a member of a transporter superfamily. *J. Virol.* **73**, 6500–5 (1999).

639 3. Brown, J. K., Fung, C. & Tailor, C. S. Comprehensive Mapping of Receptor-Functioning Domains in

640 Feline Leukemia Virus Subgroup C Receptor FLVCR1. *J. Virol.* **80**, 1742–1751 (2006).

641 4. Dutt, S., Hamza, I. & Bartnikas, T. B. Molecular Mechanisms of Iron and Heme Metabolism. *Annu.*

642 *Rev. Nutr.* **42**, 311–335 (2022).

643 5. Rajadhyaksha, A. M. *et al.* Mutations in FLVCR1 Cause Posterior Column Ataxia and Retinitis

644 Pigmentosa. *Am. J. Hum. Genet.* **87**, 643–654 (2010).

645 6. Rey, M. A. *et al.* Enhanced alternative splicing of the FLVCR1 gene in Diamond Blackfan anemia

646 disrupts FLVCR1 expression and function that are critical for erythropoiesis. *Haematologica* **93**, 1617–

647 1626 (2008).

648 7. Meyer, E. *et al.* Mutations in FLVCR2 Are Associated with Proliferative Vasculopathy and

649 Hydranencephaly-Hydrocephaly Syndrome (Fowler Syndrome). *Am. J. Hum. Genet.* **86**, 471–478

650 (2010).

651 8. Thomas, S. *et al.* High-throughput sequencing of a 4.1 Mb linkage interval reveals FLVCR2 deletions

652 and mutations in lethal cerebral vasculopathy. *Hum. Mutat.* **31**, 1134–1141 (2010).

653 9. Petrillo, S. *et al.* Endothelial cells require functional FLVCR1a during developmental and adult

654 angiogenesis. *Angiogenesis* 1–20 (2023) doi:10.1007/s10456-023-09865-w.

655 10. Santander, N. *et al.* Lack of Flvcr2 impairs brain angiogenesis without affecting the blood-brain

656 barrier. *J. Clin. Investig.* **130**, 4055–4068 (2020).

657 11. Peng, C. *et al.* FLVCR1 promotes the proliferation and tumorigenicity of synovial sarcoma through

658 inhibiting apoptosis and autophagy. *Int. J. Oncol.* **52**, 1559–1568 (2018).

659 12. Su, X. *et al.* The prognostic marker FLVCR2 associated with tumor progression and immune

660 infiltration for acute myeloid leukemia. *Front. Cell Dev. Biol.* **10**, 978786 (2022).

661    13. Yan, N. Structural Biology of the Major Facilitator Superfamily Transporters. *Annu. Rev. Biophys.*

662    **44**, 257–283 (2015).

663    14. Quigley, J. G. *et al.* Identification of a Human Heme Exporter that Is Essential for Erythropoiesis.

664    *Cell* **118**, 757–766 (2004).

665    15. Duffy, S. P. *et al.* The Fowler Syndrome-Associated Protein FLVCR2 Is an Importer of Heme. *Mol.*

666    *Cell. Biol.* **30**, 5318–5324 (2010).

667    16. Yuan, X., Protchenko, O., Philpott, C. C. & Hamza, I. Topologically Conserved Residues Direct Heme

668    Transport in HRG-1-related Proteins*. *J. Biol. Chem.* **287**, 4914–4924 (2012).

669    17. Ponka, P., Sheftel, A. D., English, A. M., Bohle, D. S. & Garcia-Santos, D. Do Mammalian Cells Really

670    Need to Export and Import Heme? *Trends Biochem. Sci.* **42**, 395–406 (2017).

671    18. Li, Y. *et al.* MFSD7C switches mitochondrial ATP synthesis to thermogenesis in response to heme.

672    *Nat. Commun.* **11**, 4837 (2020).

673    19. Bärland, N. *et al.* Mechanistic basis of choline import involved in teichoic acids and

674    lipopolysaccharide modification. *Sci. Adv.* **8**, eabm1122 (2022).

675    20. Glunde, K., Bhujwalla, Z. M. & Ronen, S. M. Choline metabolism in malignant transformation. *Nat.*

676    *Rev. Cancer* **11**, 835–848 (2011).

677    21. Jumper, J. *et al.* Highly accurate protein structure prediction with AlphaFold. *Nature* **596**, 583–589

678    (2021).

679    22. Perez, C. *et al.* Substrate-bound outward-open state of the betaine transporter BetP provides

680    insights into Na+ coupling. *Nat. Commun.* **5**, 4231 (2014).

681    23. Bazzone, A. *et al.* Investigation of sugar binding kinetics of the E. coli sugar/H+ symporter XylE

682    using solid-supported membrane-based electrophysiology. *J. Biol. Chem.* **298**, 101505 (2022).

683    24. Bazzone, A., Zerlotti, R., Barthmes, M. & Fertig, N. Functional characterization of SGLT1 using

684    SSM-based electrophysiology: Kinetics of sugar binding and translocation. *Front. Physiol.* **14**, 1058583

685    (2023).

686    25. Bazzone, A. *et al.* SSM-based electrophysiology, a label-free real-time method reveals sugar

687    binding & transport events in SGLT1. *Biosens. Bioelectron.* **197**, 113763 (2022).

688    26. Sarter, M. & Parikh, V. Choline transporters, cholinergic transmission and cognition. *Nat. Rev.*

689    *Neurosci.* **6**, 48–56 (2005).

690    27. Drew, D., North, R. A., Nagarathinam, K. & Tanabe, M. Structures and General Transport

691    Mechanisms by the Major Facilitator Superfamily (MFS). *Chem. Rev.* **121**, 5289–5335 (2021).

692    28. Martens, C. *et al.* Direct protein-lipid interactions shape the conformational landscape of

693    secondary transporters. *Nat. Commun.* **9**, 4151 (2018).

694    29. Corradi, V. *et al.* Emerging Diversity in Lipid–Protein Interactions. *Chem. Rev.* **119**, 5775–5848

695    (2019).

696    30. Zhang, X. C. & Han, L. Uniporter substrate binding and transport: reformulating mechanistic

697    questions. *Biophys. Rep.* **2**, 45–54 (2016).

698    31. Kalailingam, P. *et al.* Deficiency of MFSD7c results in microcephaly-associated vasculopathy in

699    Fowler syndrome. *J. Clin. Investig.* **130**, 4081–4093 (2020).

700    32. Schneider, K., Zimmer, D., Nielsen, H., Herrmann, J. M. & Mühlhaus, T. iMLP, a predictor for

701    internal matrix targeting-like sequences in mitochondrial proteins. *Biol. Chem.* **402**, 937–943 (2021).

702    33. O'Donoghue, N., Sweeney, T., Donagh, R., Clarke, K. J. & Porter, R. K. Control of choline oxidation

703    in rat kidney mitochondria. *Biochim. Biophys. Acta (BBA) - Bioenerg.* **1787**, 1135–1139 (2009).

704    34. Kenny, T. C. *et al.* Integrative genetic analysis identifies FLVCR1 as a plasma-membrane choline

705    transporter in mammals. *Cell Metab.* **35**, 1057-1071.e12 (2023).

706    35. Xie, T. *et al.* Rational exploration of fold atlas for human solute carrier proteins. *Structure* **30**,

707    1321-1330.e5 (2022).

708    36. Nigam, S. K. The SLC22 Transporter Family: A Paradigm for the Impact of Drug Transporters on

709    Metabolic Pathways, Signaling, and Disease. *Annu. Rev. Pharmacol. Toxicol.* **58**, 663–687 (2018).

710    37. Ueland, P. M. Choline and betaine in health and disease. *J. Inherit. Metab. Dis.* **34**, 3–15 (2011).

711    38. Zeisel, S. H. Choline: Critical Role During Fetal Development and Dietary Requirements in Adults.

712    *Annu. Rev. Nutr.* **26**, 229–250 (2006).

713    39. Goh, Y. Q., Cheam, G. & Wang, Y. Understanding Choline Bioavailability and Utilization: First Step

714    Toward Personalizing Choline Nutrition. *J. Agric. Food Chem.* **69**, 10774–10789 (2021).

715    40. Sanchez-Lopez, E. *et al.* Choline Uptake and Metabolism Modulate Macrophage IL-1β and IL-18

716    Production. *Cell Metab.* **29**, 1350-1362.e7 (2019).

717    41. Ghorbani, P. *et al.* Choline metabolism underpins macrophage IL-4 polarization and RELMα up-

718    regulation in helminth infection. (2022) doi:10.1101/2022.09.30.510305.

719    42. Bhat, S., El-Kasaby, A., Freissmuth, M. & Sucic, S. Functional and Biochemical Consequences of

720    Disease Variants in Neurotransmitter Transporters: A Special Emphasis on Folding and Trafficking

721    Deficits. *Pharmacol. Ther.* **222**, 107785–107785 (2021).

722    43. Wortmann, S. B. & Mayr, J. A. Choline-related-inherited metabolic diseases—A mini review. *J.*

723    *Inherit. Metab. Dis.* **42**, 237–242 (2019).

724    44. Mehedint, M. G., Craciunescu, C. N. & Zeisel, S. H. Maternal dietary choline deficiency alters

725    angiogenesis in fetal mouse hippocampus. *Proc. Natl. Acad. Sci.* **107**, 12834–12839 (2010).

726    45. King, J. H. *et al.* Maternal Choline Supplementation Modulates Placental Markers of Inflammation,

727    Angiogenesis, and Apoptosis in a Mouse Model of Placental Insufficiency. *Nutrients* **11**, 374 (2019).

728    46. Kwan, S. T. (Cecilia) *et al.* Maternal choline supplementation during murine pregnancy modulates

729    placental markers of inflammation, apoptosis and vascularization in a fetal sex-dependent manner.

730    *Placenta* **53**, 57–65 (2017).

731    47. Jin, X., Wang, R., Wang, H., Long, C. & Wang, H. Brain protection against ischemic stroke using

732    choline as a new molecular bypass treatment. *Acta Pharmacol. Sin.* **36**, 1416–1425 (2015).

733    48. Irobi, J., Jonghe, P. D. & Timmerman, V. Molecular genetics of distal hereditary motor

734    neuropathies. *Hum. Mol. Genet.* **13**, R195–R202 (2004).

735    49. Wang, H. *et al.* Choline transporter mutations in severe congenital myasthenic syndrome disrupt

736    transporter localization. *Brain* **140**, 2838–2850 (2017).

737    50. Fagerberg, C. R. *et al.* Choline transporter-like 1 deficiency causes a new type of childhood-onset

738    neurodegeneration. *Brain* **143**, 94–111 (2019).

739    51. Bauché, S. *et al.* Impaired Presynaptic High-Affinity Choline Transporter Causes a Congenital

740    Myasthenic Syndrome with Episodic Apnea. *Am. J. Hum. Genet.* **99**, 753–761 (2016).

741    52. Cruz, P. M. R. *et al.* Presynaptic congenital myasthenic syndrome due to three novel mutations in

742    SLC5A7 encoding the sodium-dependant high-affinity choline transporter. *Neuromuscul. Disord.* **31**,

743    21–28 (2021).

744    53. Bazzone, A., Barthmes, M. & Fendler, K. Chapter Two SSM-Based Electrophysiology for

745    Transporter Research. *Methods Enzym.* **594**, 31–83 (2017).

746    54. Bazzone, A. & Barthmes, M. Functional Characterization of SLC Transporters Using Solid

747    Supported Membranes. *Methods Mol. Biol. (Clifton, NJ)* **2168**, 73–103 (2020).

748    55. Punjani, A., Rubinstein, J. L., Fleet, D. J. & Brubaker, M. A. cryoSPARC: algorithms for rapid

749    unsupervised cryo-EM structure determination. *Nat. Methods* **14**, 290–296 (2017).

750    56. Zheng, S. Q. *et al.* MotionCor2: anisotropic correction of beam-induced motion for improved cryo-

751    electron microscopy. *Nat. Methods* **14**, 331–332 (2017).

752    57. Zhang, K. Gctf: Real-time CTF determination and correction. *J. Struct. Biol.* **193**, 1–12 (2016).

753    58. Bepler, T. *et al.* Positive-unlabeled convolutional neural networks for particle picking in cryo-

754    electron micrographs. *Nat. methods* **16**, 1153–1160 (2019).

755    59. Scheres, S. H. W. RELION: Implementation of a Bayesian approach to cryo-EM structure

756    determination. *J. Struct. Biol.* **180**, 519–530 (2012).

757    60. Kimanius, D., Dong, L., Sharov, G., Nakane, T. & Scheres, S. H. W. New tools for automated cryo-

758    EM single-particle analysis in RELION-4.0. *Biochem. J.* **478**, 4169–4185 (2021).

759    61. Emsley, P., Lohkamp, B., Scott, W. G. & Cowtan, K. Features and development of Coot. *Acta*

760    *Crystallogr. Sect. D* **66**, 486–501 (2010).

761    62. Croll, T. I. ISOLDE: a physically realistic environment for model building into low-resolution

762    electron-density maps. *Acta Crystallogr. Sect. D, Struct. Biol.* **74**, 519–530 (2018).

763    63. Goddard, T. D. *et al.* UCSF ChimeraX: Meeting modern challenges in visualization and analysis:

764    UCSF ChimeraX Visualization System. *Protein Sci.* **27**, 14–25 (2017).

765    64. Adams, P. D. *et al.* PHENIX: a comprehensive Python-based system for macromolecular structure

766    solution. *Acta Crystallogr. Sect. D, Biol. Crystallogr.* **66**, 213–21 (2009).

767    65. Chen, V. B. *et al.* MolProbity: all-atom structure validation for macromolecular crystallography.

768    *Acta Crystallogr. Sect. D: Biol. Crystallogr.* **66**, 12–21 (2010).

769    66. Abraham, M. J. *et al.* GROMACS: High performance molecular simulations through multi-level

770    parallelism from laptops to supercomputers. *SoftwareX* **1**, 19–25 (2015).

771    67. Jo, S., Kim, T., Iyer, V. G. & Im, W. CHARMM-GUI: A web-based graphical user interface for

772    CHARMM. *J. Comput. Chem.* **29**, 1859–1865 (2008).

773    68. Huang, J. *et al.* CHARMM36m: an improved force field for folded and intrinsically disordered

774    proteins. *Nat. Methods* **14**, 71–73 (2017).

775    69. Khan, H. M., MacKerell, A. D. & Reuter, N. Cation-π Interactions between Methylated Ammonium

776    Groups and Tryptophan in the CHARMM36 Additive Force Field. *J. Chem. theory Comput.* **15**, 7–12

777    (2018).

778    70. Essmann, U. *et al.* A smooth particle mesh Ewald method. *J. Chem. Phys.* **103**, 8577–8593 (1995).

779    71. Hess, B., Bekker, H., Berendsen, H. J. C. & Fraaije, J. G. E. M. LINCS: A linear constraint solver for

780    molecular simulations. *J. Comput. Chem.* **18**, 1463–1472 (1997).

781    72. Berendsen, H. J. C., Postma, J. P. M., Gunsteren, W. F. van, DiNola, A. & Haak, J. R. Molecular

782    dynamics with coupling to an external bath. *J. Chem. Phys.* **81**, 3684–3690 (1984).

783    73. Evans, D. J. & Holian, B. L. The Nose–Hoover thermostat. *J. Chem. Phys.* **83**, 4069–4074 (1985).

784    74. Parrinello, M. & Rahman, A. Polymorphic transitions in single crystals: A new molecular dynamics

785    method. *J. Appl. Phys.* **52**, 7182–7190 (1981).

786    75. Humphrey, W., Dalke, A. & Schulten, K. VMD: Visual molecular dynamics. *J. Mol. Graph.* **14**, 33–38

787    (1996).

788    76. Michaud-Agrawal, N., Denning, E. J., Woolf, T. B. & Beckstein, O. MDAnalysis: a toolkit for the

789    analysis of molecular dynamics simulations. *J. Comput. Chem.* **32**, 2319–27 (2010).

790    77. Sehnal, D. *et al.* MOLE 2.0: advanced approach for analysis of biomacromolecular channels. *J.*

791    *Cheminformatics* **5**, 39–39 (2013).

792    78. Tian, W., Chen, C., Lei, X., Zhao, J. & Liang, J. CASTp 3.0: computed atlas of surface topography of

793    proteins. *Nucleic Acids Res.* **46**, W363–W367 (2018).

794    79. Sievers, F. *et al.* Fast, scalable generation of high-quality protein multiple sequence alignments

795    using Clustal Omega. *Mol. Syst. Biol.* **7**, 539–539 (2011).

796
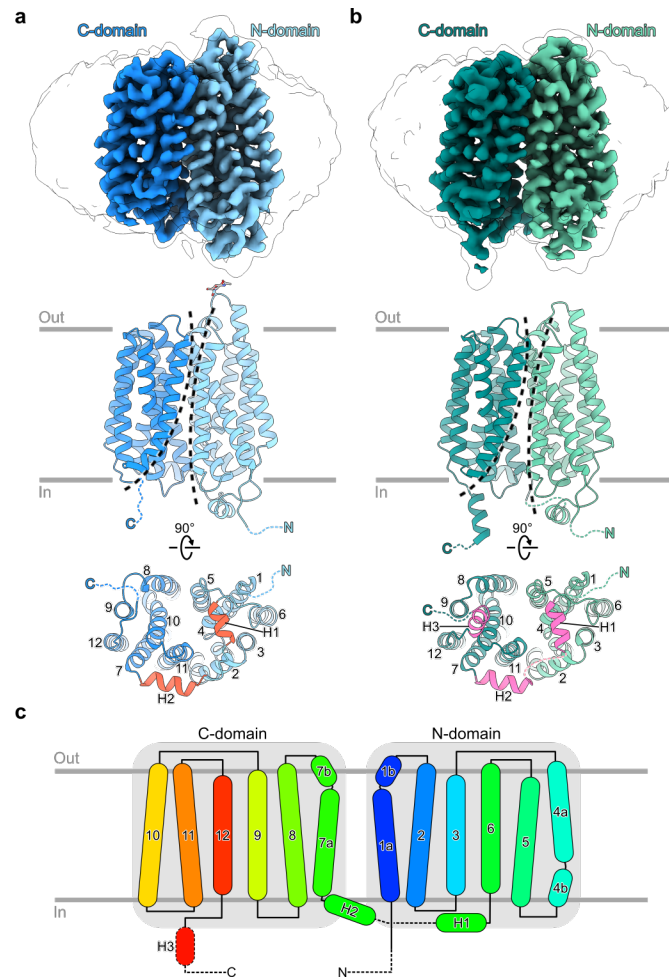
**Fig. 1: Cryo-EM structures of FLVCR1 and FLVCR2 in their inward-facing state.**

Cryo-EM density (top) and atomic model (middle and bottom) of inward-facing FLVCR1 (**a**), and inward-facing FLVCR2 (**b**). The N- and C-domains are coloured in different shades of blue and green for FLVCR1 and FLVCR2, respectively. A transparent cryo-EM density lowpass-filtered at 6 Å is shown to visualize the detergent belt surrounding the transmembrane region. The internal view (bottom) shows the arrangement of TMs, with inner side helices highlighted in orange (FLVCR1) or pink (FLVCR2). The sidechain of N265 in FLVCR1 and its N-linked glycan (grey) are shown as stick models. **c**, Schematic diagram of FLVCR family showing the topology of the secondary structure. Motifs that are not observed in both cryo-EM structures of FLVCR1 and FLVCR2 are shown as dashed lines.

808
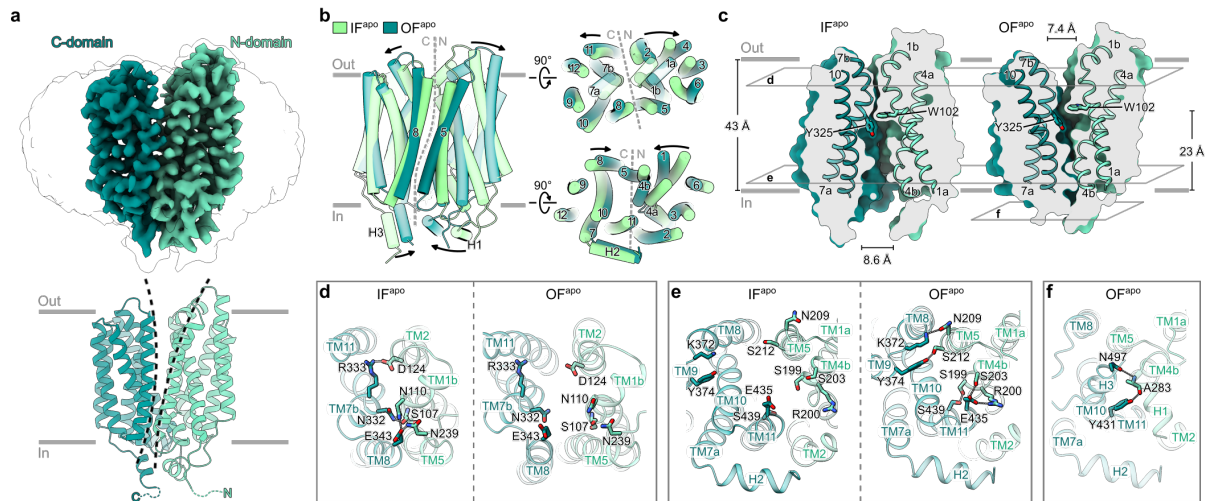
**Fig. 2: Structural heterogeneity and gating mechanism of FLVCR2.**

**a**, Cryo-EM density (top) and atomic model (bottom) of outward-facing FLVCR2. **b**, Structural superposition of FLVCR2-OF$^{apo}$ (dark green) and FLVCR2-IF$^{apo}$ (light green). **c**, Cut-away views of the surface representation showing the cavity shape of FLVCR2-IF$^{apo}$ (left) and FLVCR2-OF$^{apo}$ (right). Two central aromatic residues are shown as sticks. Cross-sections of inter-domain interactions in FLVCR2-IF$^{apo}$ (left) and FLVCR2-OF$^{apo}$ (right) are shown from the external (**d**), or from the internal side (**e**). **f**, Internal view of FLVCR2-OF$^{apo}$ showing the inter-domain interactions between H1 and H3. Residues participating in the inter-domain interactions are shown as sticks; hydrogen bonds and salt bridges are labelled with dashed lines.

818

819
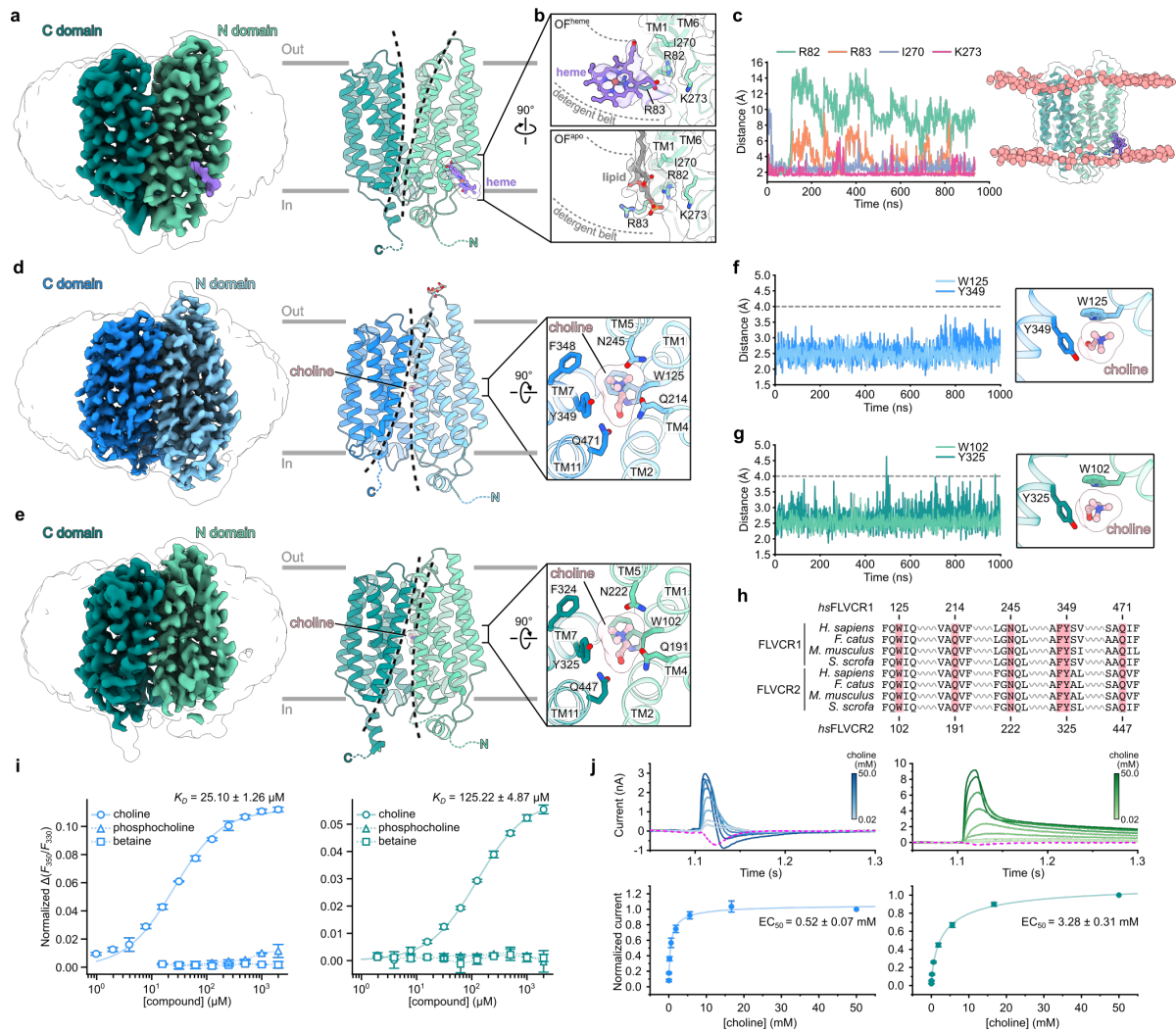
**Fig. 3: Cryo-EM structures of FLVCR1 and FLVCR2 in complex with choline and heme.**

**a**, Cryo-EM density (left) and ribbon model (right) of the heme-bound outward-facing FLVCR2 (FLVCR2-OF$^{heme}$). The heme molecule is shown in ball-and-stick representation, and the corresponding cryo-EM density is coloured in purple. **b**, Close-up views of the heme-binding site in FLVCR2-OF$^{heme}$ (top) and in FLVCR2-OF$^{apo}$ (bottom) with locally-filtered cryo-EM density. Residues in close proximity to heme are shown as sticks. A lipid molecule (grey ball-and-stick) is fitted into the lipid-like density at the heme-binding site of FLVCR2-OF$^{apo}$. **c**, Time-resolved distance plot between heme and interacting residues from MD experiments are shown. A snapshot of FLVCR2-heme interaction during the simulation is shown. For simplicity, only the phosphates of POPE/POPG are shown as red spheres. **d,e**, Cryo-EM densities and atomic models of the choline-bound inward-facing FLVCR1 (FLVCR1-IF$^{choline}$) structure, and the choline-bound inward-facing FLVCR2 (FLVCR2-IF$^{choline}$) structure, respectively. The bound choline is shown as ball-and-stick model; binding site residues are shown as sticks. **f,g**, Time-resolved

832     distance plots between choline and the highly-conserved tryptophan and tyrosine residues forming the

833     choline-binding pockets of FLVCR1 (**f**) and FLVCR2 (**g**) obtained from MD simulation runs. A cation-π

834     interaction is assumed for distance <4 Å (grey dashed line). **h**, Protein sequence alignment of choline-

835     binding pocket residues (red block) in FLVCR1 and FLVCR2 across various mammalian species. Indicated

836     residue numbers refer to FLVCR1 and FLVCR2 from *homo sapiens*. **i**, Choline-binding affinity of FLVCR1

837     (left) and FLVCR2 (right) determined by nanoDSF. Data are represented as mean ± standard deviation

838     (s.d.; *n* = 3). **j**, Representative choline-induced current traces of FLVCR1 (left) or FLVCR2 (right)

839     containing proteoliposomes. Representative current traces of protein-free liposomes induced by 50

840     mM choline are shown as magenta dashed lines. Data are represented as mean ± s.d. (*n* = 4).

841
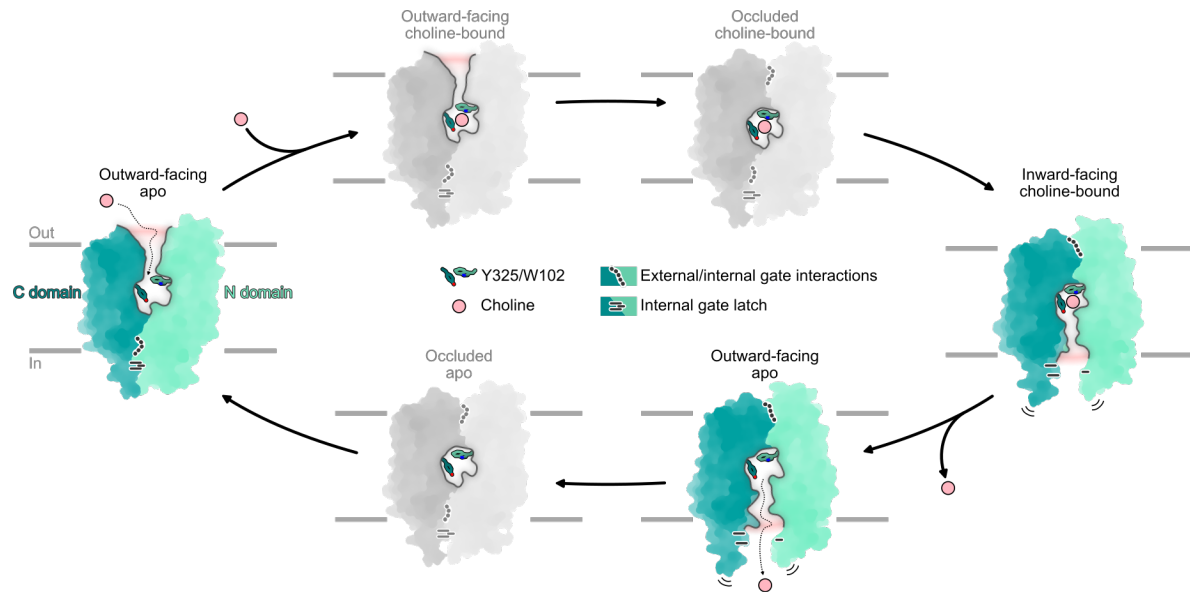
**Fig. 4: Proposed model for choline transport by FLVCR2.**

Schematic illustration of FLVCR2 conformations during the choline transport cycle. Green-coloured states represent experimentally obtained conformations in this study. States coloured in grey are hypothesized based on knowledge about the commonly characterized alternative-access mechanism of MFS transporters.

849
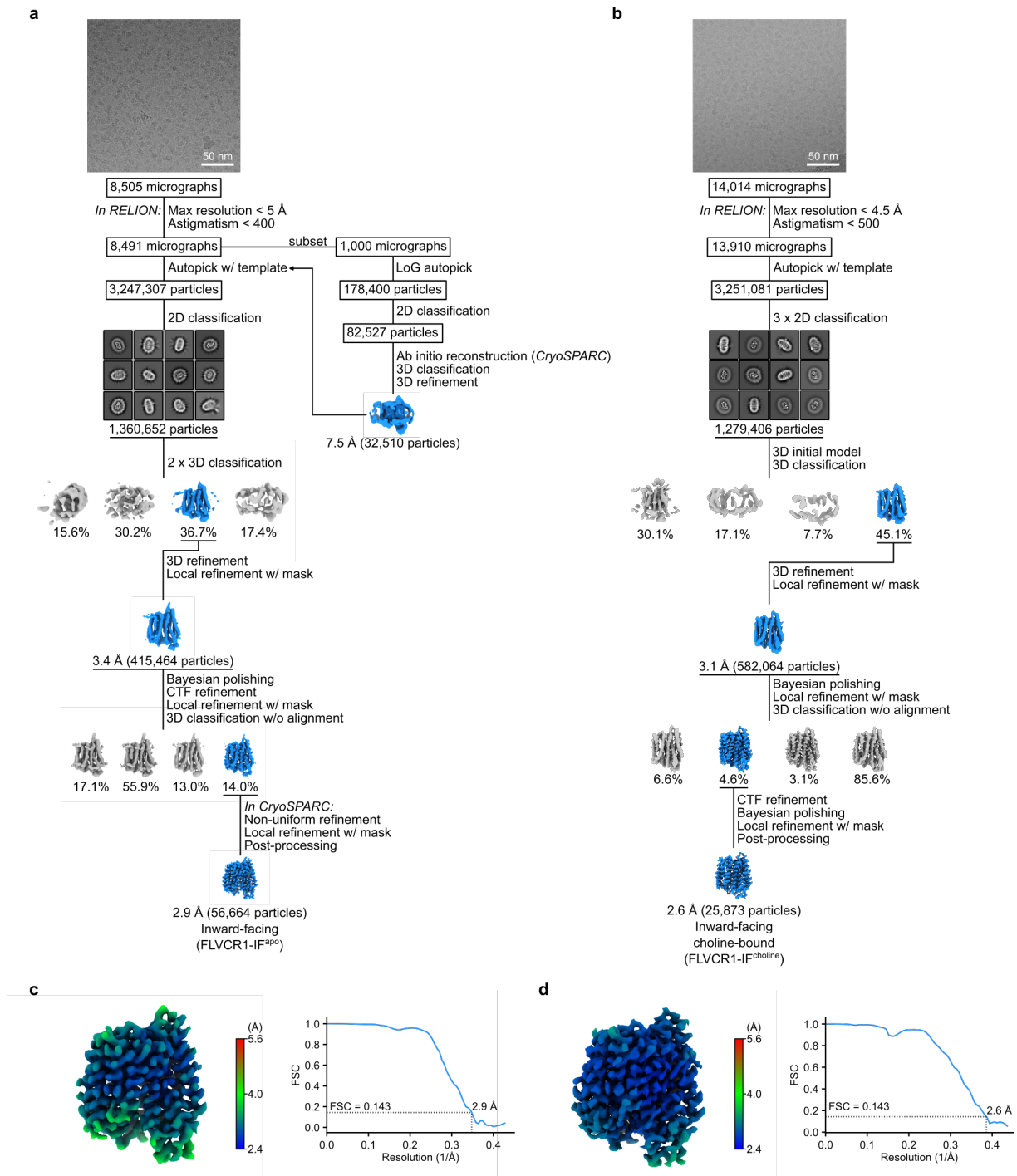
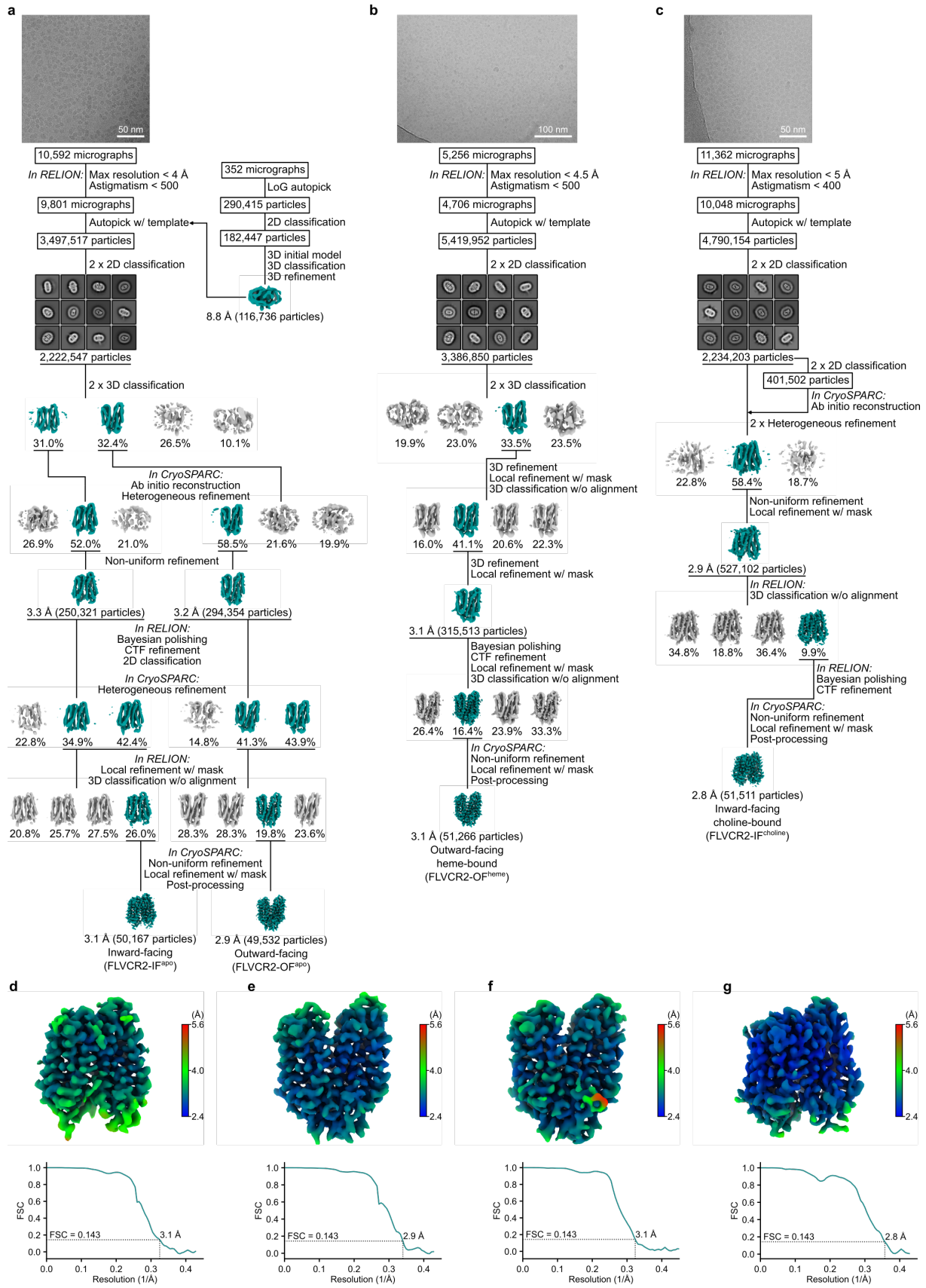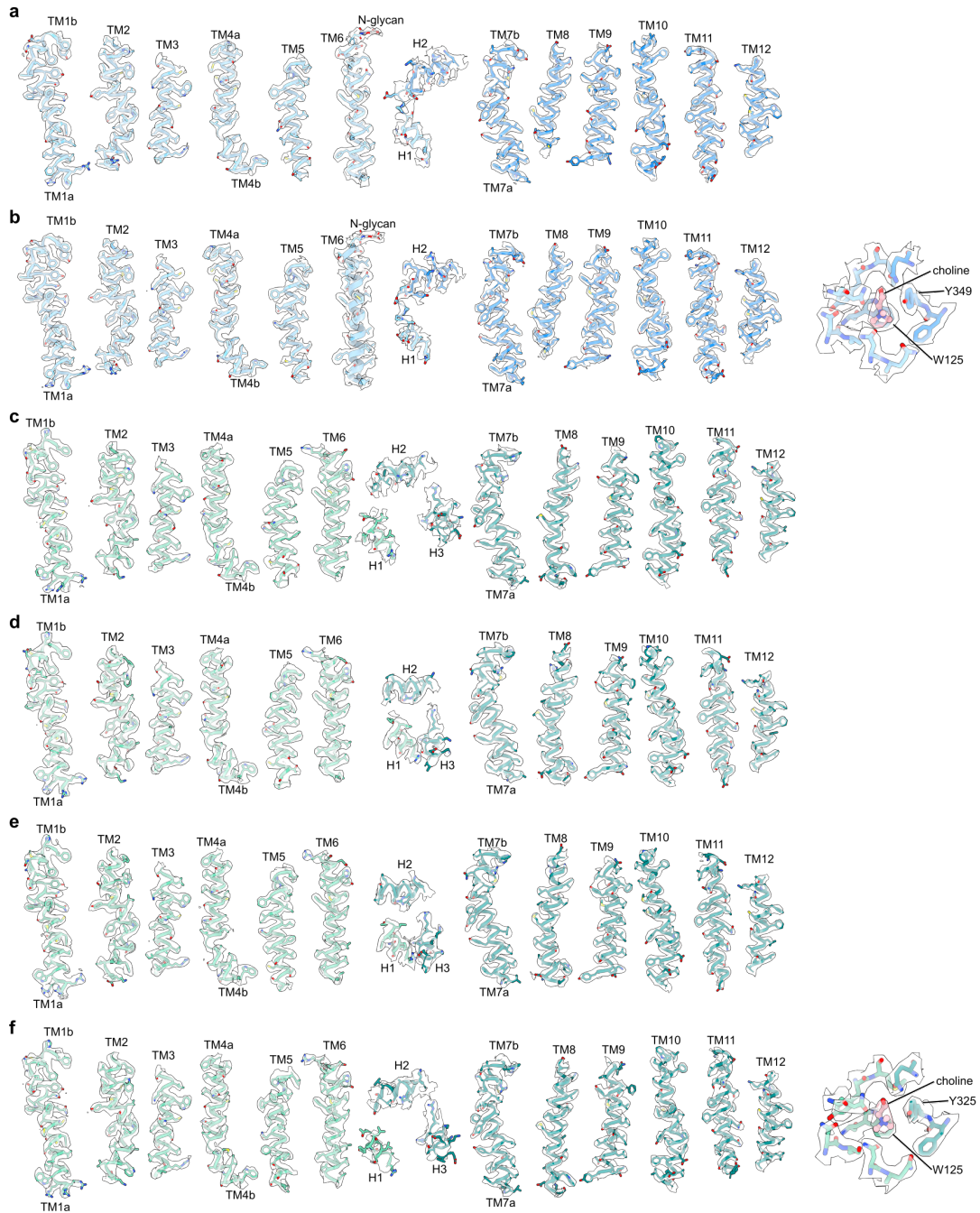**Extended Data Fig. 1: Single-particle cryo-EM analysis of human FLVCR1.**

**a,b**, Summary of the data processing procedure of the as-isolated FLVCR1 sample and FLVCR1 supplemented with choline. **c,d**, Local resolution estimation (left) and Fourier shell correlation (FSC) curves (right) of the final cryo-EM maps of FLVCR1-IF$^{apo}$ and -IF$^{choline}$.
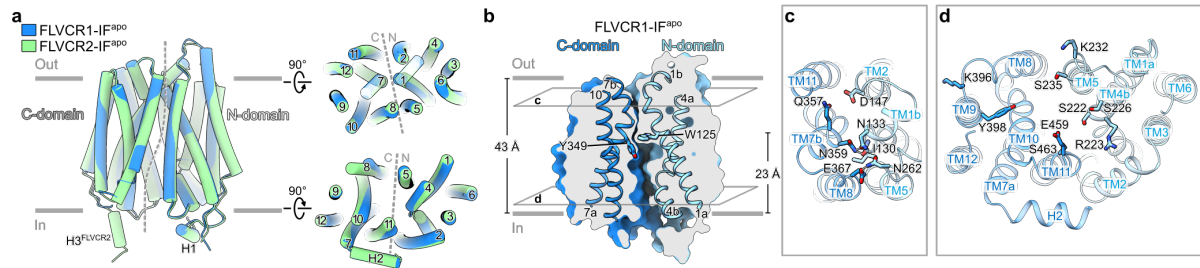
854

855

**Extended Data Fig. 2: Single-particle cryo-EM analysis of human FLVCR1.**

857    **a-c**, Summary of the data processing procedure of the as-isolated FLVCR2, heme-supplemented, and

858    choline-supplemented FLVCR2 samples. **d-g**, Local resolution estimation (top) and FSC curves (bottom)

859    of the final cryo-EM maps of FLVCR2-IF$^{apo}$, FLVCR2-OF$^{apo}$, FLVCR2-OF$^{heme}$, and FLVCR2-IF$^{choline}$.

860

**Extended Data Fig. 3: Cryo-EM density and model fitting.**

Cryo-EM map and model fits of the transmembrane and intracellular helices of FLVCR1-IF$^{apo}$ (**a**), FLVCR1-IF$^{choline}$ (**b**), FLVCR2-IF$^{apo}$ (**c**), FLVCR2-OF$^{apo}$ (**d**), FLVCR2-OF$^{heme}$ (**e**), and FLVCR2-IF$^{choline}$ (**f**). The map for choline and the surrounding residues is shown for the choline-bound states of FLVCR1 and FLVCR2, respectively.

868

**Extended Data Fig. 4: Structural comparison between FLVCR1-IF<sup>apo</sup> and FLVCR2-IF<sup>apo</sup>.**

**a**, Structural comparison of FLVCR1-IF<sup>apo</sup> and FLVCR2-IF<sup>apo</sup> in tube representation, viewed from the lipid bilayer (left), extracellular side (top-right), and intracellular side (bottom-right). **b**, Cut-away view of FLVCR1-IF<sup>apo</sup> in surface representation showing the cytoplasmic cavity. Two central aromatic residues are shown as sticks. **c,d**, Cross-sections of inter-domain interactions in FLVCR1-IF<sup>apo</sup> as indicated in (**b**), viewed from the extracellular side (**c**), or from the intracellular side (**d**). Residues corresponding to the inter-domain interaction residues in FLVCR2 are shown.

876

**Extended Data Fig. 5: Chemicophysical properties of FLVCR structures and conservation analyses.**

Surface charge, hydrophobicity, and conservation analyses of FLVCR1-IF[apo] (**a**), FLVCR1-IF[choline] (**b**), FLVCR2-IF[apo] (**c**), FLVCR2-OF[apo] (**d**), and FLVCR2-IF[choline] (**e**). From left to right: Surface viewed from the lipid bilayer and both C and N domains viewed from the domain interface coloured by electrostatic potential, the domain interface coloured by hydrophobicity, and the domain interface coloured by

883    sequence conservation. The cavity in the different states of both FLVCRs is outlined with dashed lines.

884    Two important central pocket residues (W125 and Y349 in FLVCR1; W102 and Y325 in FLVCR2) are

885    indicated.

886
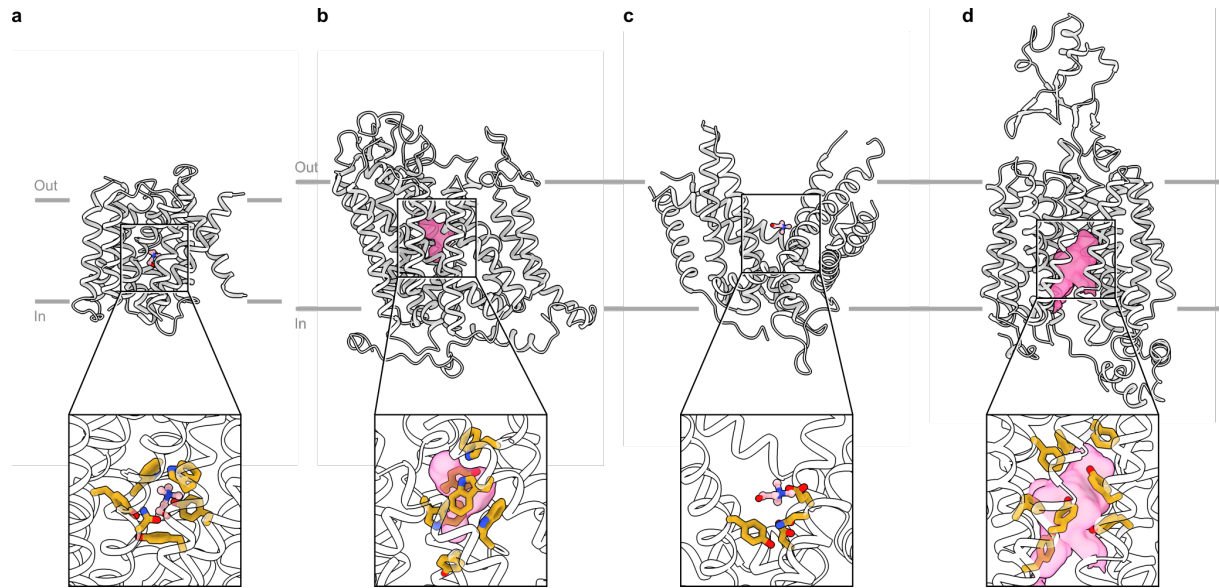
**Extended Data Fig. 6: Structures of bacterial and mammalian choline transporters.**

Experimental or predicted structures of bacterial choline transporter LicB (PDB 7B0K; **a**) and other known human choline transporters SLC5A7 (AlphaFold AF-Q9GZV3-F1; **b**), SLC44A1 (PDB 7WWB; **c**), and SLC22A5 (AlphaFold AF-O76082-F1; **d**). The lower panels show the close-up views of their respective binding sites. Choline or putative choline-binding cavities are highlighted in pink. Choline-binding residues or residues lining a putative choline-binding site are indicated in yellow.

893

894
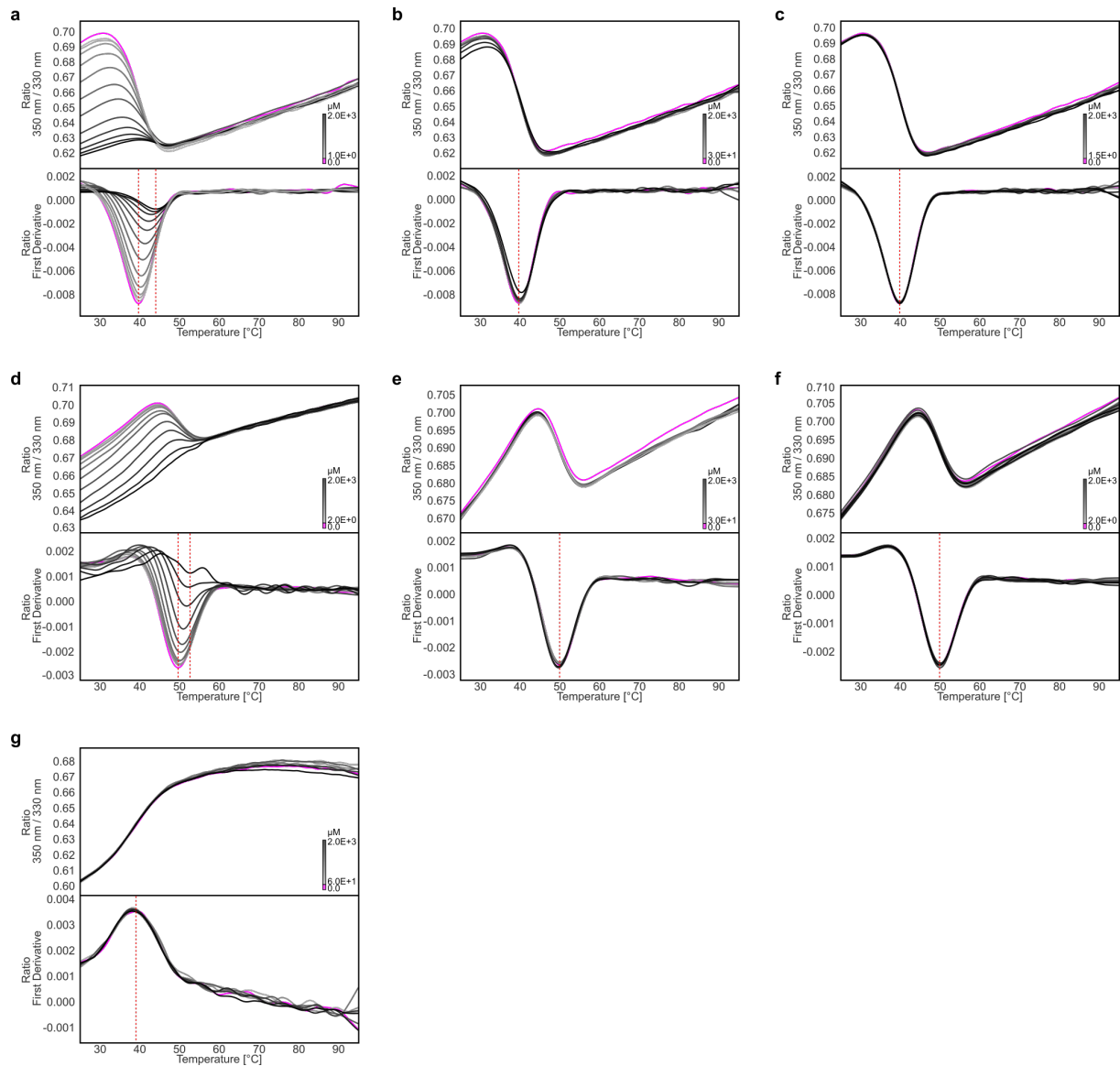
**Extended Data Fig. 7: Binding affinity screening of FLVCRs in the presence of choline or its metabolites by nano differential scanning fluorimetry (nanoDSF).**

**a-c**, Representative nanoDSF measurements ($F_{350}/F_{330}$) along a temperature ramp from 25°C to 95°C (top) and the respective first derivative (bottom) of detergent-solubilized FLVCR1 and FLVCR2 in the presence of a serial dilution of choline (**a,d**), phosphocholine (**b,e**), or betaine (**c,f**). **g**, Representative negative-control assay using a purified human sodium transporter from the SLC9 family in the presence of a serial dilution of choline. Magenta lines represent measurements of the samples without choline. Red vertical dashed lines represent the melting temperatures of the samples without choline and the samples of FLVCRs with 2 mM choline.
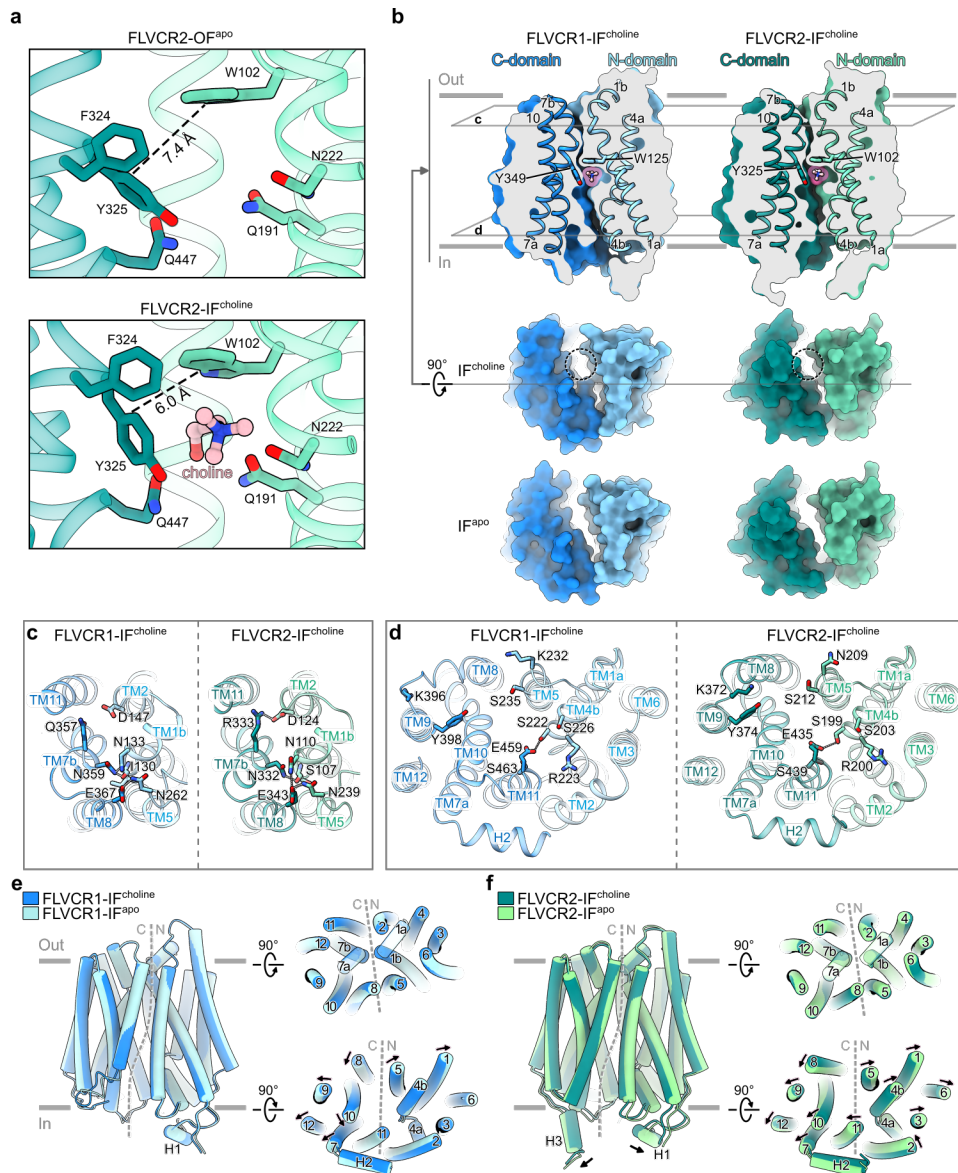
904
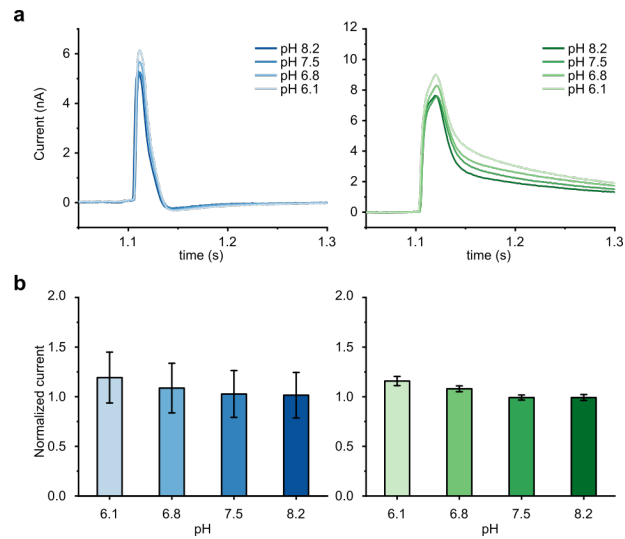
**Extended Data Fig. 8: SSM-based electrophysiological profiles of FLVCRs in proteoliposomes.**

**a**, Current traces for FLVCR1 (left) or FLVCR2 (right) proteoliposomes with buffers at different pH as indicated in the figure. **b**, Normalized peak currents for FLVCR1 (left) and FLVCR2 (right) based on the measurement in (**a**). Data are represented as mean ± s.d. ($n = 4$).

911

912 **Extended Data Fig. 9: Structural comparison of FLVCRs in their choline-bound inward-facing states.**

913 **a**, Choline-binding sites of FLVCR2-OF$^{apo}$ (top) and FLVCR2-IF$^{choline}$ (bottom) with the distance between

914 W102 and Y325 shown as dashed lines. **b**, Cut-away views of FLVCR1-IF$^{choline}$ (top-left) and FLVCR2-

915 IF$^{choline}$ (top-right) showing the inward-facing cavity. Two central aromatic residues are shown as sticks.

916 The surfaces shown below are the IF$^{apo}$ and IF$^{choline}$ states of FLVCR1 (left) and FLVCR2 (right) viewed

917 from the internal side. The dashed circles indicate the peripheral channel in the choline-bound state.

918 **c,d**, Cross-sections of inter-domain interactions in FLVCR1-IF$^{choline}$ (left) and FLVCR2-IF$^{choline}$ (right) as

919 indicated in (**b**), viewed from the external side (**c**), or from the internal side (**d**). **e**, Structural comparison

920    of FLVCR1-IF$^{choline}$ and FLVCR1-IF$^{apo}$, viewed from the lipid bilayer (left), external side (top-right), and

921    internal side (bottom-right). **h**, Structural comparison of FLVCR2-IF$^{choline}$ and FLVCR2-IF$^{apo}$, viewed from

922    the lipid bilayer (left), external side (top-right), and internal side (bottom-right).

923
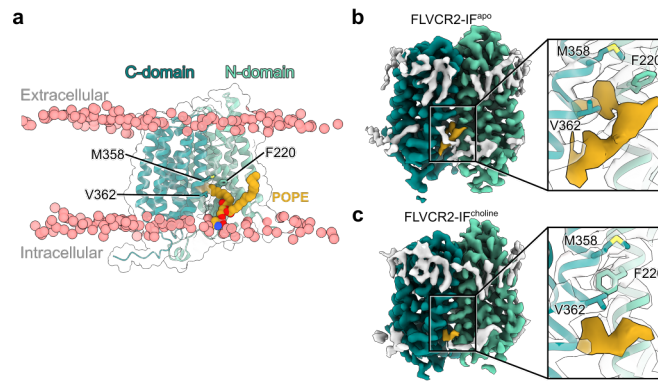
**Extended Data Fig. 10: Lateral gate in the inward-facing state of FLVCR2.**

**a**, An MD-snapshot of FLVCR2 in the inward-facing state showing the entry of a lipid acyl group into the lateral gate in the cytoplasmic leaflet. The POPE molecule is shown in yellow and heteroatom colour codes. For simplicity, only the phosphates of the other POPE/POPG are shown as red spheres. **b,c,** Cryo-EM density maps of FLVCR-IF$^{apo}$ and -IF$^{choline}$ in viewing angle of the lipid-binding site. The lipid/detergent density is coloured grey. Lipid/detergent density entering the lateral gate is shown in yellow. The three residues at the lateral gate are shown as stick models.

931
932